Advanced Functional Materials

ADVANCED FUNCTIONAL MATERIALS
www.afm-journal.de

RESEARCH ARTICLE OPEN ACCESS

Bioinspired Polypeptide Dendrimer-Modified Thin-Film Composite Membranes for Selective Lithium-Magnesium Separation with DFT Insights

Mehrasa Yassari[1] | Seyedeh Fatemeh Seyedpour[1] | Bamlak Setegne[1] | Amir Aghaei[1,2] | Behzad Ahvazi[3] | Mostafa Dadashi Firouzjaei[1,4] | Mark Elliott[4] | Mohtada Sadrzadeh[1]

[1]Department of Mechanical Engineering, 10-241 Donadeo Innovation Center for Engineering, Advanced Water Research Lab (AWRL), University of Alberta, Edmonton, Alberta, Canada | [2]Quantum and Nanotechnology Research Centre, National Research Council Canada (NRC), Edmonton, Alberta, Canada | [3]Canna Stream Solutions Ltd. (CSS), Edmonton, Alberta, Canada | [4]Department of Civil, Construction, and Environmental Engineering, University of Alabama, Tuscaloosa, Alabama, USA

Correspondence: Mohtada Sadrzadeh (sadrzade@ualberta.ca)

Received: 20 October 2025 | **Revised:** 7 December 2025 | **Accepted:** 16 December 2025

Keywords: biomimetic nanofiltration membrane | density functional theory | lithium-magnesium separation | polypeptide dendrimer | thin-film composite membrane

ABSTRACT

Selective ion transport in nanofiltration (NF) enables sustainable lithium (Li^+) recovery. While many membranes rely on strong positive charge for Li^+/Mg^{2+} separation, we show that negatively charged membranes can also excel using a biomimetic approach. Inspired by biological ion channels that achieve cation selectivity via specific binding sites despite their negative charge, we designed a nitrogen-rich polypeptide dendrimer (amino acid–based) bearing carboxylate coordination sites with higher affinity for Mg^{2+} than Li^+, while moderating the membrane's net negative charge. This biomimetic design enhanced Li^+ recovery by inhibiting Mg^{2+} transport through stronger interactions, thereby allowing for preferential Li^+ permeation. This process occurred through a combination of electrostatic modulation and ligand-assisted coordination. Density functional theory (DFT) calculations indicated strong oxygen-donor coordination: lysine motifs bind hydrated Mg^{2+} ($E \approx -170$ kcal.mol^{-1}) far more strongly than Li^+ ($E \approx -50.2$ kcal.mol^{-1}). The optimized membrane achieved Li^+/Mg^{2+} selectivity of 15.6 at neutral pH with 23 LMH flux, and 136 at pH 4, highlighting strong performance in acidic feeds. Long-term tests showed ~0.4% leaching over 10 days with stable rejection and enrichment of Li^+ (feed Li^+/Mg^{2+} increased from 0.05 to 0.20). Antifouling tests showed a twofold lower flux-decline ratio and higher flux-recovery than the unmodified TFC.

1 | Introduction

The demand for lithium, driven by the rapid growth of lithium-ion batteries and supercapacitors [1], is projected to rise by over 30% annually across various energy sectors, reaching nearly three times the 2018 level by 2025 [2, 3]. Since over 60% of current lithium production originates from brine resources, the co-existence of lithium ions (Li^+) and magnesium ions (Mg^{2+}), along with the typically high Mg^{2+}/Li^+ ratio, remains a major challenge for efficient extraction [4, 5]. Conventional approaches, such as adsorption, chemical precipitation, electrolysis, and solvent extraction, often suffer from low selectivity and limited flux, resulting in poor Li^+ recovery [6, 7]. These practical constraints, coupled with the scale of projected demand, motivate the search for separation platforms that can deliver both high throughput and ion specificity.

Compared to conventional techniques, membrane-based separation offers a more energy-efficient and environmentally friendly approach with high throughput [8–10]. Nanofiltration (NF) membranes, in particular, are attractive due to their suitable molecular weight cut-off (200–400 Da) and tunable surface charge, enabling the separation of monovalent and divalent cations via size exclusion and Donnan exclusion [11]. Thin-film composite (TFC) NF membranes have gained increasing attention due to their simple fabrication method, rapid interfacial polymerization (IP) process, and mild reaction conditions [12, 13]. Typically, conventional TFC membranes for monovalent/divalent separation are prepared through IP between amine-rich monomers such as piperazine (PIP) or polyethyleneimine (PEI) and trimesoyl chloride (TMC) [14]. This architecture provides a practical foundation for tuning charge and microstructure, but it also exposes key limits when ionic composition and strength depart from idealized conditions.

Specifically, because the hydrated radii of Mg^{2+} (0.42 nm) and Li^{+} (0.38 nm) in aqueous media [15, 16] are similar, size exclusion alone cannot achieve effective separation. Recognizing that conventional TFC membranes are negatively charged, researchers have introduced positively charged functionalities to enhance Li^{+}/Mg^{2+} selectivity via Donnan exclusion [17–19], either by incorporating amine-rich monomers during IP or by post-synthesis grafting and secondary IP [20–22]. Hydrated and protonated amine groups increase surface positive charge, repelling Mg^{2+}, while allowing Li^{+} transport. However, most reported membranes still exhibit low water flux, poor chemical stability in complex brines, and inadequate Li^{+}/Mg^{2+} selectivity under realistic conditions, primarily because Donnan exclusion is weakened in high-ionic-strength brines, where electrostatic screening and competing ions diminish charge-based selectivity [17, 23]. Additional limitations include the low content of amine-containing monomers, overly dense polyamide (PA) networks, particularly those formed with branched polymers like PEI due to their high degree of crosslinking, and the absence of a specific chemical affinity for Li^{+} over Mg^{2+} [24, 25]. For example, Lu et al. [25] observed strong Li^{+} rejection for a positively charged PEI-based NF membrane, highlighting the lack of selective affinity for Li^{+}. Moreover, surface modifications with amines or zwitterions can introduce added mass-transfer resistance, further reducing water flux [26]. Although prior studies have clarified how surface charge and nanoscale architecture govern ion transport, substantive improvements in Li^{+}/Mg^{2+} selectivity are unlikely without introducing high-affinity coordination sites that discriminate Li^{+} from Mg^{2+} beyond simple Donnan (charge) exclusion.

To address this gap, researchers have drawn inspiration from biological ion channels and protein systems that pair precise pore architectures with well-placed functional groups to achieve selective coordination [27]. For instance, carboxylate-functionalized nanochannels have been shown to enhance the permeation of water and cations due to their negative charge [28]. Furthermore, incorporating sulfonate groups, such as sodium 4-styrene sulfonate (PSS), into MXene membranes was found to improve Li^{+}/Mg^{2+} selectivity through favorable coordination [29]. Other strategies employ metal-organic frameworks (MOFs), covalent-organic frameworks (COFs), porous organic frameworks (POFs), and crown ethers to create ion-selective conduits [30–35]. Recent TFN strategies incorporating MOFs have also demonstrated improved ion separation by enhancing surface charge and introducing adsorption-based affinity sites [36–38]. Ethylenediamine tetraacetic acid (EDTA)-modified membranes have also been explored, but their performance is dominated by Donnan exclusion rather than coordination-driven selectivity, resulting in limited discrimination between multivalent ions [39, 40]. Crown-ether functionalization provides defined cavity binding, but the synthesis is complex, transport is tightly constrained by fixed pore geometry, and the chemistry typically offers only a single oxygen-donor environment [41, 42].

In contrast, our dendrimer presents a molecularly defined coordination interface composed of both nitrogen and oxygen-donor groups, and its ion selectivity properties can be tuned via pH-dependent protonation, an adaptability absent in the above systems. This dynamic control over charge density and coordination environment enables higher selectivity, particularly under acidic conditions. However, many existing TFN systems require nanoparticle incorporation rather than relying on well-defined molecular interfacial chemistry. Moreover, many synthetic pores lack sufficient internal free volume, mechanical robustness, or long-term chemical stability to sustain high-flux, durable separations under harsh brine conditions. These limitations motivate an alternative design principle: decouple ion recognition from bulk pore geometry and engineer the membrane-solution interface itself to perform the “decision-making”.

Therefore, instead of further tailoring the pore geometry, we conferred ion recognition capability on the membrane surface by grafting a nitrogen-rich polypeptide dendrimer onto the polyamide active layer, creating dense, tunable coordination sites and charged, biomimetic nanochannels [43–48]. Specifically, the TFC polyamide was functionalized with an L-arginine (Arg)/L-lysine (Lys)-based dendrimer that provides oxygen-donor sites. At neutral pH, protonated guanidinium/amine groups together with deprotonated carboxylates form a zwitterionic interface that electrostatically excludes co-ions while transiently coordinating hydrated cations, thereby enabling Li^{+}/Mg^{2+} selectivity [31, 49–55]. To expand and tune the coordination chemistry, we further introduced 2,4,6-triaminopyrimidine (TAP) as a nitrogen-donor ligand, providing a direct contrast to the oxygen-donor sites and adjustable binding strength [56–59].

Inspired by ligand-gated ion channels [60–65], this surface modification yields a biomimetic, ion-selective interface governed by the synergy of electrostatic screening and specific coordination. This design rationale is further supported by well-established ion-selectivity mechanisms in biological channels. In ligand-gated and voltage-gated ion channels, acidic residues such as aspartate and glutamate often form bidentate carboxylate bridges that regulate Ca^{2+}, Na^{+}, and K^{+} permeation through charge-dense coordination sites [61, 66]. Similarly, sulfonate (SO_3^{-}) motifs have been shown to create Li^{+} selective pathways by enhancing electrostatic attraction [62]. Nucleophilic residues such as cysteine and tyrosine also contribute to metal binding through soft-donor interactions, shaping the local chemical environment of the pore [63]. In addition, glycine-rich regions modulate steric constraints and local charge density, further influencing ion discrimination [60]. These biomimetic principles guided our selection of dendrimer segments capable of providing tunable coordination chemistry and charge-regulated selectivity. Natural Ca^{2+} selective channels also rely on clusters of aspartate and

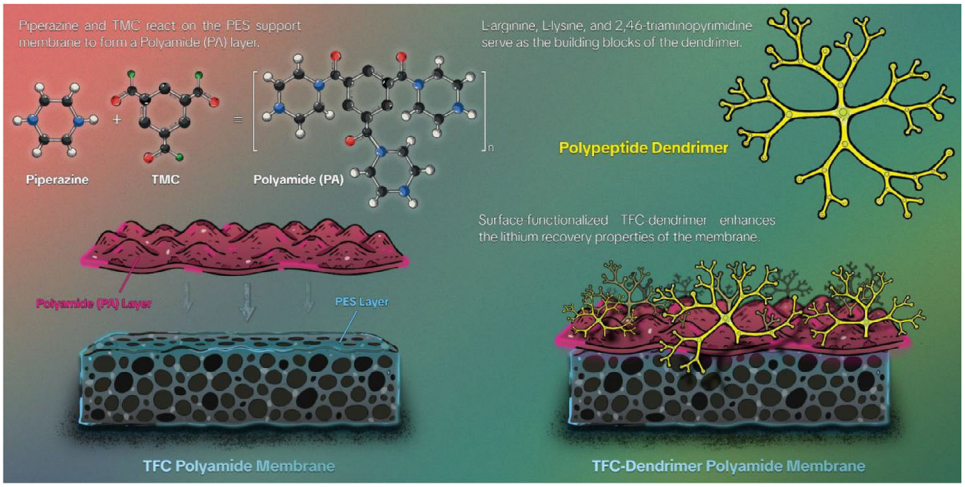

FIGURE 1 | Schematic illustration of fabricated membranes with their morphological structure. Carbon atoms are represented in black, nitrogen in blue, oxygen in red, and hydrogen in white.

glutamate residues that create strong local electrostatic fields and enforce partial dehydration of permeating cations [67]. A similar principle is expected here, where the pH-dependent protonation of Arg/Lys/TAP establishes a tunable local charge environment that modulates Li^+ and Mg^{2+} transport analogously.

Density functional theory (DFT) calculations were employed to quantify binding preferences, hydration perturbations, and coordination geometries at the modified surface, helping to interpret the molecular contribution to Li^+/Mg^{2+} separation [68–70].

2 | Materials and Methods

2.1 | Chemicals and Materials

Polyether sulfone (PES, Solvay Advanced Polymers), polyvinylpyrrolidone (PVP, Mw = 360 kDa, Sigma–Aldrich), Triton X-100 (Merck), polyethylene glycol (PEG, Mw = 2000 Da), and N, N-dimethylacetamide (DMAc, Fisher Scientific) were used for the fabrication of the PES support layer. TMC, PIP (≥99%), triethylamine (TEA), sodium hydroxide (NaOH), and n-hexane were all purchased from Sigma-Aldrich and used for the preparation of TFC membranes. The polypeptide dendrimer was synthesized from aminoterephthalic acid (NH_2-BDC), trimesic acid (BTC), Arg, Lys, and TAP (Sigma-Aldrich). Ethanol (99%, Fisher Scientific) and deionized (DI) water were used as solvents for solution preparation. Glutaraldehyde solution (GA, 25 wt.%) was used as a crosslinker. PEG with molecular weights between 100 Da and 2000 Da was used for MWCO measurements of the membranes. Anhydrous pyridine, deuterated chloroform, cyclohexanol, chromium (III) acetylacetonate, and the phosphitylating reagent 2-chloro-4,4,5,5-tetramethyl-1,3,2-dioxaphospholane (TMDP) were used for ^{31}P NMR measurements. All of these chemicals were of HPLC grade and purchased from Sigma–Aldrich.

Different salts obtained from Fisher Scientific were used to assess membrane performance, including lithium chloride (LiCl), magnesium chloride hexahydrate ($MgCl_2.6H_2O$, 97%, Fisher), potassium chloride (KCl, Fisher), sodium chloride (NaCl, Fisher), magnesium sulfate ($MgSO_4$), and sodium sulfate (Na_2SO_4). For fouling studies, sodium alginate (SA 12–80 kDa, Sigma–Aldrich) was selected as a model organic foulant. The antifouling properties of the membranes were evaluated in the presence of calcium chloride ($CaCl_2$, Fisher Scientific).

2.2 | Synthesis and Characterization of Polypeptide Dendrimer

Appropriate amounts of NH_2-BDC (0.81 g), TAP (1.22 g), BTC (2.04 g), Arg (3.52 g), and Lys (2.41 g) were dissolved in a mixture of 200 mL of DI water and 400 mL of ethanol in a 1,000 mL round-bottomed flask. The resulting mixture was sonicated for 20 min in an ultrasonic bath and stirred for 2 h. The suspension was then refluxed at its boiling point for 18 h and cooled to room temperature. The precipitate was filtered and then washed three times with a 300 mL ethanol: water mixture (70:30), followed by centrifugation to remove any unreacted compounds. The obtained material was then dried in the oven at 60°C. The synthesized dendrimer was characterized using various techniques as described in the Supporting Information.

2.3 | Fabrication of PES Support Layer

The PES support membrane was fabricated by the non-solvent induced phase separation (NIPS) method via the immersion precipitation technique [71]. More details are provided in the Supporting Information.

2.4 | Fabrication of Pristine and Dendrimer-Modified TFC Membranes (TFC and TFC-Den)

Pristine TFC was formed on PES by interfacial polymerization of an aqueous PIP (1.2 wt.%) solution containing NaOH (0.15 wt.%) and TEA (0.5 wt.%) (soak 2 min), followed by contact with TMC

(0.1 wt.%) in n-hexane (30 s) and thermal cure at 80°C for 5 min [72]. The TFC-Den$_x$ membranes were obtained by coating the PA layer with different amounts of dendrimer (X = 0.5–3.0 wt.%, 4 min), followed by GA (1 wt.%, 2 min) crosslinking and post-curing in an oven (80 °C, 5 min). All membranes were stored in DI water before testing. Detailed procedures are provided in the Supporting Information. The structural and chemical properties of TFC and TFC-Den membranes were characterized using multiple analytical techniques as described in the Supporting Information. A schematic representation of the surface-functionalized TFC membrane and its proposed selective ion transport pathway is shown in Figure 1, illustrating the overall design concept.

2.5 | Evaluation of Membrane Separation Performance

Flux and rejection of all TFC and TFC-Den membranes were measured using a lab-scale cross-flow filtration system (Sterlitech Corp., USA). Single salt experiments were conducted using feed solutions containing 1,000 ppm $MgCl_2$ and 1,000 ppm LiCl. Binary salt and long-term stability experiments were conducted using a feed solution of $MgCl_2$ and LiCl (total concentrations of 1,000 ppm and a fixed Li^+/Mg^{2+} molar ratio of 1:20). All experiments were performed in triplicate to minimize potential variability, and the mean values are reported. Detailed calculations, performance procedures, and additional MWCO, fouling, and release stability tests are provided in the Supporting Information.

2.6 | Molecular-Level Insights via DFT Calculations

The chemical characteristics of the synthesized dendrimer and its interactions with hydrated cations were investigated using DFT, a quantum mechanical modeling method. All DFT calculations were performed with the ORCA quantum chemistry software (version 6.0.1) [73–75]. Molecular geometries and hydrated complexes were optimized using the B3LYP hybrid functional with D3BJ dispersion correction and def2-SVP basis set. To improve computational efficiency, the RIJCOSX approximation was applied throughout the calculations [76–80].

The chemical structures were built in Avogadro software [81]. Post-processing calculations, including molecular electrostatic potential (ESP) analysis and frontier molecular orbital (HOMO-LUMO) analysis, were conducted using the Multiwfn program (version 3.7) [82], based on ORCA electron density outputs. The ESP maps were visualized in Avogadro to interpret the spatial distribution of electrostatic potential and potential ion-interaction sites. Details are provided in the Supporting Information.

3 | Results and Discussions

3.1 | Dendrimer Characterization and Structural Features

The chemical composition and functional groups of the synthesized dendrimer were studied by attenuated total reflectance Fourier transform infrared spectroscopy (ATR-FTIR) and X-ray photoelectron spectroscopy (XPS) (Figure S1a–e). Characteristic amide I and amide II bands at 1680 and 1554 cm^{-1}, together with XPS C 1s, N 1s, and O 1s signals, verified the presence of amide linkages and nitrogen-rich functionalities, confirming the successful synthesis of the dendrimer. Phosphorus-31 nuclear magnetic resonance (^{31}P NMR) of the soluble fraction showed resonances at 148 and 142 ppm, indicating the presence of hydroxyl functionalities within the dendrimer backbone, while signals expected for carboxyl groups were not observed (Figure S1g).

The zeta potential measurements revealed that the polypeptide dendrimer exhibited a negative surface charge of −13.9 mV under neutral conditions (pH 7). This negative potential was attributed to the ionization of carboxyl functional groups distributed on the dendrimer surface, which promoted electrostatic repulsion and thereby enhanced colloidal stability, modulating interactions with surrounding molecules and solvent systems.

Field-emission scanning electron microscopy (SEM) and transmission electron microscopy (TEM) (Figures S1h$_1$–i$_2$) revealed hyperbranched, cubic-like morphologies in the submicron to micron size range. SEM images showed cubic-tetragonal structures (~300–500 nm in cross-section and up to 5 μm in length), while TEM confirmed a hyperbranched network of dendritic branches 50–200 nm in diameter (additional information provided in the Supporting Information). EDX mapping (Figure S1j$_1$–j$_4$) further verified the presence of carbon (C), nitrogen (N), and oxygen (O), consistent with the amino acid composition of the dendrimer.

3.2 | Characterization of Membranes

3.2.1 | Chemical Composition and Functional Groups

FTIR and XPS analyses of the fabricated membranes were performed to monitor the changes in the chemical composition and functional groups of the pristine TFC membrane upon dendrimer modification (Figure S2a–i). In the FTIR analysis of the dendrimer-coated membrane (TFC-Den$_2$), the increased intensity of the amide II bond at 1575 cm^{-1}, along with higher nitrogen and oxygen content in XPS, confirmed successful dendrimer coating on the polyamide layer of TFC. Detailed chemical composition of TFC and TFC-Den$_2$, including the XPS survey and high-resolution XPS deconvolution, is provided in the Supporting Information.

3.2.2 | Surface Properties and Charge

To investigate the impact of dendrimer incorporation on membrane hydrophilicity, water contact angle (WCA) measurements were performed for both unmodified and dendrimer-coated membranes, as shown in Figure 2a. The results illustrated enhanced hydrophilicity after dendrimer modification, decreasing from 54.5° for TFC to 37.7° for TFC-Den$_2$.

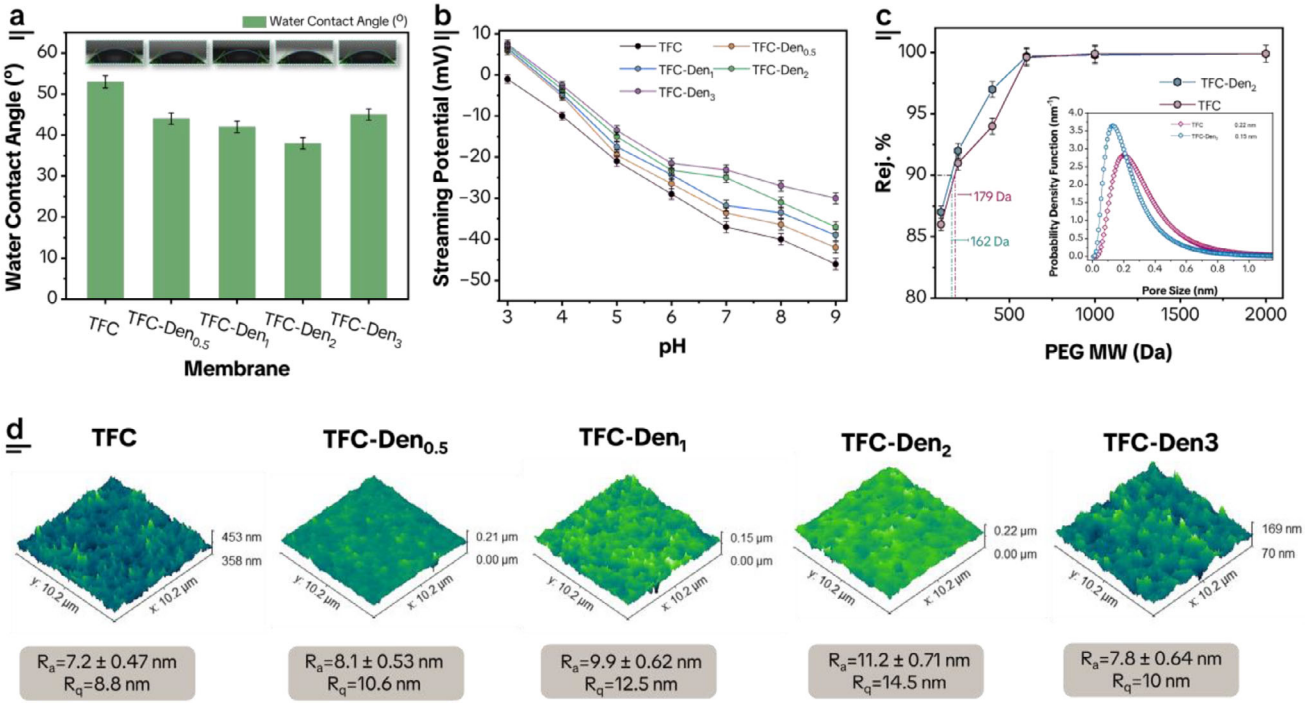

FIGURE 2 | Surface characterization of membranes. (a) WCA measurements indicated improved hydrophilicity after dendrimer coating, (b) Streaming potential profiles over the pH 3–9 showed a reduction in negative surface charge, (c) MWCO rejection curves exhibited minor differences in size exclusion between the unmodified TFC and dendrimer-coated TFC-Den$_2$ membranes, with the pore size distribution shown as an inset, revealing a reduced mean pore size of 0.15 nm for TFC-Den$_2$, and (d) 3D AFM images showed subtle increase in surface roughness following dendrimer modification.

3.2.3 | Morphological Analysis

Streaming potential measurements (pH 3–9) revealed that dendrimer-modified membranes carried a less negative surface charge than pristine TFC. At low pH, the zeta potential approached around 7 mV, reflecting protonation of the dendrimer's amine groups (Figure 2b).

The 3D atomic force microscopy (AFM) images were obtained, and roughness parameters, including average roughness (R_a) and root-mean-square roughness (R_q), were quantified (Figure 2d). As a result of dendrimer modification, the surface average roughness increased slightly from 7.2 nm (TFC) to a maximum of 11.2 nm (TFC-Den$_2$), then decreased to 7.8 nm (TFC-Den$_3$). This trend was consistent with the WCA results, where increased surface roughness contributed to enhanced hydrophilicity [83].

To complement the surface analysis, MWCO and pore size distribution analysis were performed to evaluate changes in pore size and distribution (Figure 2c). According to the results, the calculated MWCO decreased from 179 Da (TFC) to 162 Da (TFC-Den2), corresponding to mean pore sizes of 0.22 and 0.15 nm, respectively (Figure 2c,d). Further details on membrane surface properties and charge are provided in the Supporting Information.

SEM and TEM analyses revealed that dendrimer modification progressively introduced nanoscale globular surface structures on top of the TFC layer (Figure 3a) while maintaining a distinct PA selective layer of around 260 nm thickness (Figure 3b). At higher dendrimer loadings, spherical surface features became evident, consistent with dendrimer coverage and the formation of aggregates. Compared to the unmodified TFC, the PA layer exhibited higher image contrast after incorporating the dendrimer. In TEM, higher contrast indicates reduced electron transmission through the specimen, which is typically associated with increased mass-thickness or local scattering density [84]. Thus, the observed contrast enhancement suggests that the selective layer became more densely packed due to interactions between the dendrimer and polyamide.

3.3 | DFT Prediction of the Synthesized Dendrimer for Li^+/Mg^{2+} Separation

DFT calculations were performed to investigate how different segments of the synthesized dendrimer contributed to the molecular-level separation of Li^+ and Mg^{2+} ions (Figure 4). This study aimed to provide insight into the interactions between potential coordination sites of Arg, Lys, and TAP with Li^+ and Mg^{2+}, which exhibit distinct coordination preferences. These insights help guide the design of dendrimers with tunable affinity toward each ion. To evaluate their contributions to selective coordination, descriptors such as interaction energy, Mulliken charge distribution, and frontier molecular orbital energies were calculated for each ligand segment in both the unbound and metal-coordinated states.

The intrinsic electrophilic or nucleophilic properties of ligands were first assessed via ESP analysis. ESP maps helped to visualize molecular polarity and identify the reactive centers for metal coordination [85]. Gas-phase ESP maps, together with HOMO-

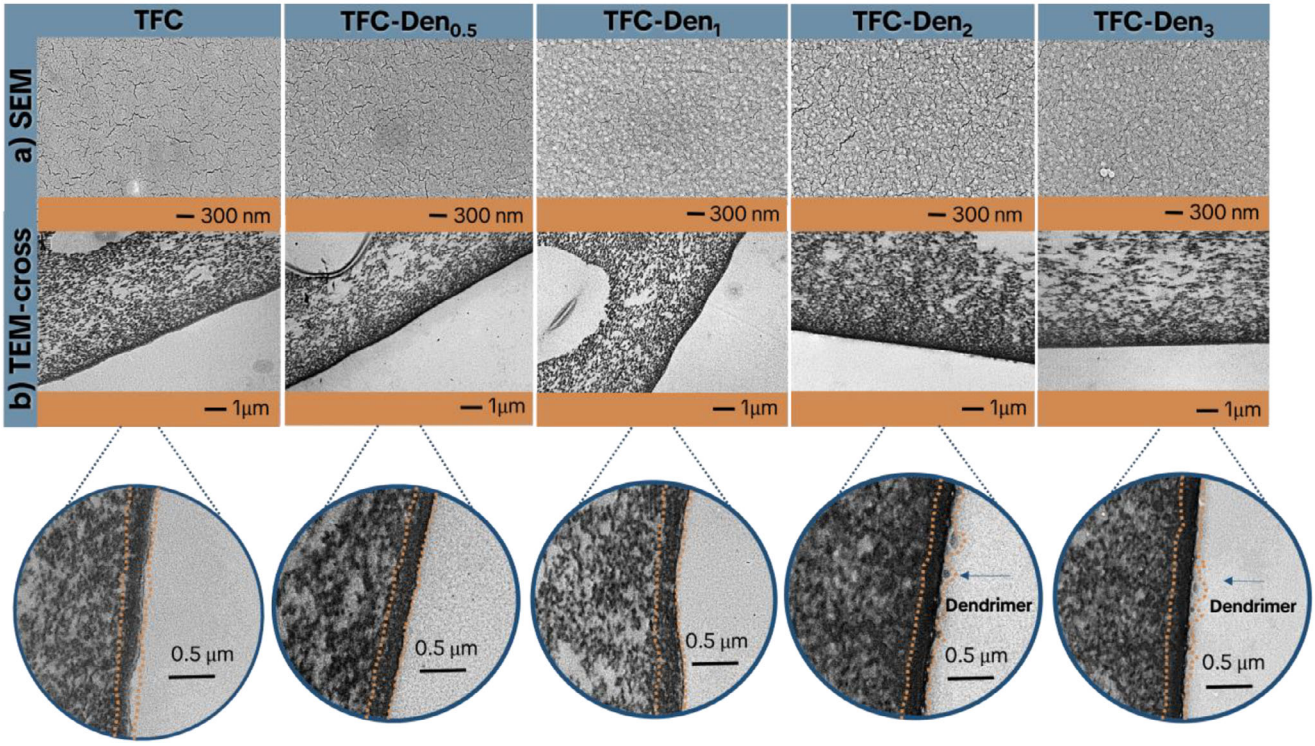

FIGURE 3 | Surface morphology of membranes. (a) Top-surface SEM images revealed mild, progressive changes in surface features with increasing dendrimer concentration, and (b) Cross-sectional TEM images confirmed the presence of a dendrimer layer. At higher concentrations, the dendrimer appeared as globular features on top of the TFC layer, whereas changes were minimal at lower concentrations.

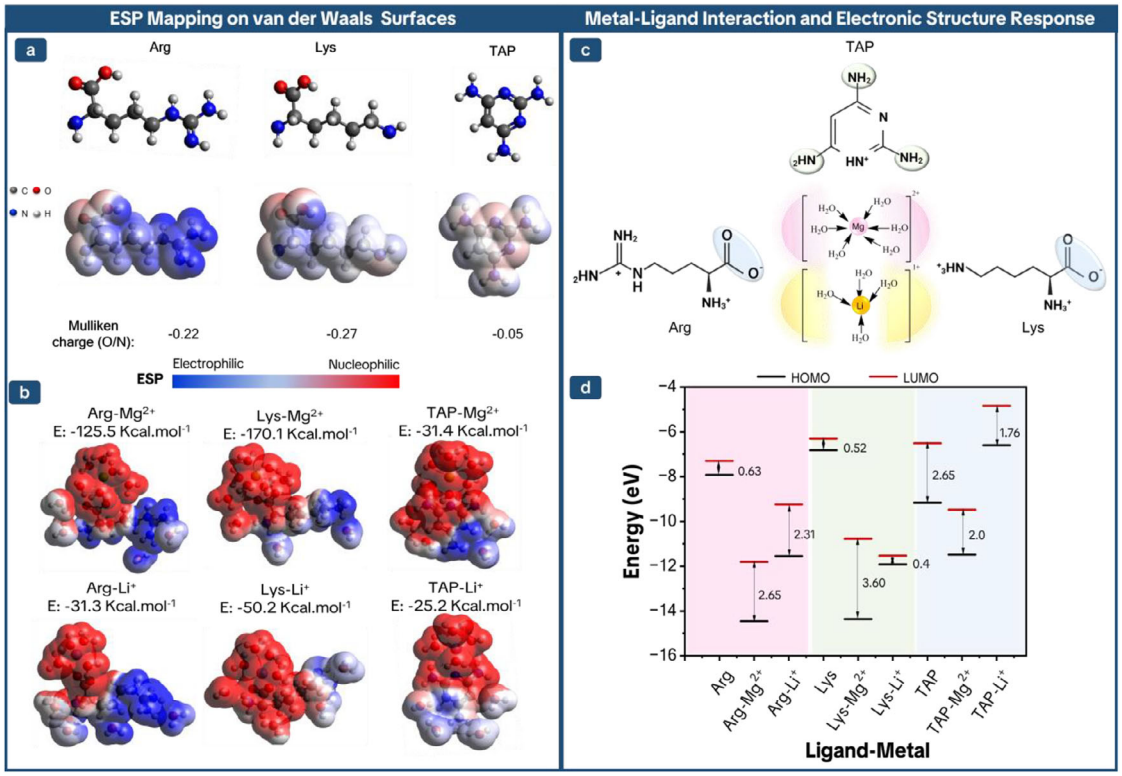

FIGURE 4 | DFT calculations of the dendrimer and its building blocks for (a) Gas-phase ESP maps over van der Waals surfaces and Mulliken atomic charges were calculated for individual dendrimer components in the absence of metal interaction, (b) Aqueous-phase ESP maps and interaction energies were determined following coordination with hydrated metal complexes, (c) Illustration of potential interaction sites, including oxygen-donor and nitrogen-donor groups, involved in coordinating with hydrated metal ions, and (d) HOMO-LUMO energy gaps of dendrimer components were calculated in unbound and metal-bound hydrated states, with Lys showing the highest chemical reactivity (smallest energy gap) among all the ligands.

TABLE 1 | Calculated characteristics of metal-ligand pairs in aqueous phase, using hydrated, charged model systems at pH 7.

Ligand-Metal Complex	Mulliken Charge/Electron		Mayer Bond Order	Bond Length (Å)
	Metal (Mg^{2+}/Li^{+})	Electron Donor (O/N)		
Arg-Mg^{2+}	+0.28	−0.17	0.66	2.7
Arg-Li^{+}	+0.32	−0.21	0.26	1.9
Lys-Mg^{2+}	+0.25	−0.21	0.68	2.2
Lys-Li^{+}	+0.31	−0.25	0.28	1.85
TAP-Mg^{2+}	+0.13	−0.07	0.18	3.6
TAP-Li^{+}	+0.43	−0.03	0.14	3.1

LUMO energy gaps and Mulliken charge analysis, were generated for the neutral isolated Arg, Lys, and TAP segments to provide a qualitative view of their inherent electron-donor and electron-acceptor tendencies in the absence of solvation. These calculations served only as a baseline for identifying likely coordination sites. To study the behavior under conditions relevant to the membrane environment, all subsequent DFT calculations, including aqueous-phase ESP, Mulliken charges, HOMO-LUMO energies, interaction energies, and Mayer bond orders and bond lengths, were performed in the hydrated state at pH 7 using solvated and charged model systems. In these hydrated models, each ligand was assigned its expected protonation state at pH 7, and metal ions (Li^{+} and Mg^{2+}) were represented with their corresponding hydration shells. This framework allows us to distinguish intrinsic ligand properties from their coordination behavior in solution, and to interpret metal-ligand interactions under chemically realistic conditions.

The increasing order of ESP was indicated by the color bar, progressing from red to blue. The white region corresponds to areas where ESP is zero or near-zero. ESP mapping in Figure 4a indicates distinct coordination characteristics among the ligands. Lys and Arg showed electron-rich regions (red) around their oxygen-donor sites and electron-deficient regions (blue) near protonated nitrogen atoms, indicating their potential for metal coordination primarily through oxygen functionalities. In contrast, TAP demonstrated the weakest coordination capacity through its nitrogen-donor sites. This was also consistent with its surface in the model system, which appeared less polarized compared to Lys and Arg. Although Arg exhibited a more pronounced ESP gradient due to a stronger internal dipole, its guanidinium group could form intramolecular salt bridges, limiting metal access. In contrast, Lys showed a more diffuse ESP distribution, but the absence of strong intramolecular stabilization left its oxygen-donor sites more exposed, enabling more effective charge transfer [52].

In the hydrated state, ESP hydrated Mg^{2+} (octahedral) and Li^{+} (tetrahedral) ions were coordinated with the hydrated individual dendrimer segments. Specifically, the deprotonated carboxylate groups (COO^{-}) of lysine (Lys) and arginine (Arg) acted as the primary metal-coordinating sites at neutral pH. At this pH, the amine groups of both amino acids were protonated (NH_3^{+}), and the molecules existed in their zwitterionic forms. For TAP, partial protonation of the ring nitrogen occurred at pH 7, allowing the unprotonated NH_2 groups to act as electron-donating sites (Figure 4c) [86].

Upon coordination (as shown in Figure 4b), all ligands showed increased polarization on their ESP surfaces, especially near the metal-binding sites, indicating stronger electronic interactions and greater charge transfer potential, particularly for Mg^{2+} complexes. Among all ligands, TAP displayed a gentler ESP gradient, reflecting lower polarization and weaker electron-donating ability, consistent with its nitrogen-donor character. For Li^{+} complexes, all ligands exhibited reduced ESP polarization due to the lower electrostatic potential of the monovalent ion. These calculated data illustrate that gas-phase ESP helps identify donor sites, while hydrated state ESP mapping reveals the actual electrostatic environment and coordination potential under physiologically relevant conditions. Table 1 summarizes data obtained from DFT calculations in the aqueous phase.

The electronic structure calculations showed that both Mg^{2+} and Li^{+} interact more strongly with oxygen-donor ligands (Lys and Arg) compared to nitrogen-donor TAP, predicting the dominant role of carboxylate oxygen in coordination. The extent of charge transfer, bond order, and interaction energies consistently indicated that Mg^{2+} forms more stable complexes than Li^{+}, particularly with Lys, due to its higher charge density and stronger electrostatic attraction. These results are consistent with the observed experimental trends. Comprehensive analyses of Mulliken charge redistribution, bond length variations, Mayer bond order, and HOMO-LUMO energy levels are presented in the Supporting Information.

3.4 | Separation Performance of the Fabricated Membranes

3.4.1 | Performance in Single and Binary Feed Solutions

The ion rejection and flux performance of the dendrimer-modified membranes were evaluated in both single-salt and binary-salt systems and compared with those of the pristine TFC membrane. Experiments were conducted using 1000 ppm solutions of LiCl and $MgCl_2$, as well as a binary feed with a Li^{+}/Mg^{2+} molar ratio of 1:20. As the concentration of dendrimer increased from TFC-$Den_{0.5}$ to TFC-Den_3, a steady decrease in flux

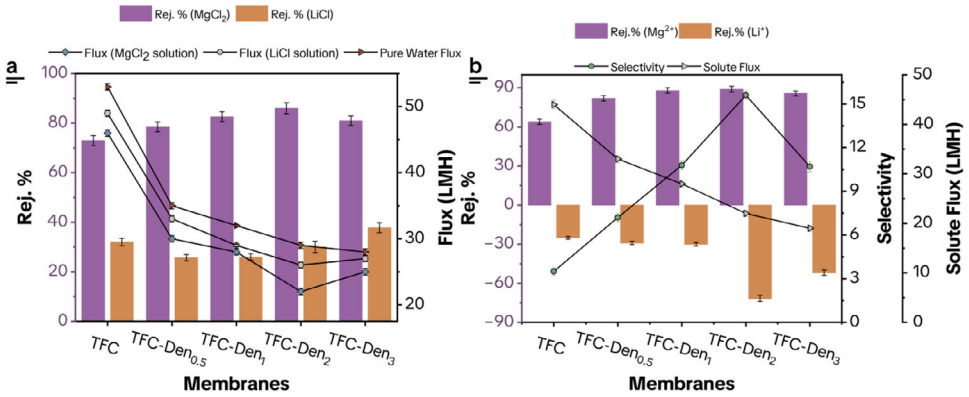

FIGURE 5 | Separation performance of membranes. (a) Rejection of $MgCl_2$ and LiCl in a single salt feed solution (1000 ppm each) at pH 7, and (b) Rejection of Mg^{2+} and Li^+ in a binary salt feed solution with a total concentration of 1000 ppm and a Li^+/Mg^{2+} molar ratio of 1:20 at pH 7. All measurements were conducted in triplicate (n = 3); error bars represent standard deviation.

was observed for both pure water and salt solutions (Figure 5a). This decline suggests that the dendrimer layer forms an effective surface coating, adding interfacial resistance to mass transfer and slightly reducing pore accessibility. This interpretation is supported by both XPS and EDX results (Supporting Information), which show an increase in nitrogen and a slight decrease in oxygen after grafting, supporting that the modification remains confined near the surface.

In single salt experiments, $MgCl_2$ rejection improved with the addition of the dendrimer. The highest rejection (86%) was achieved by TFC-Den$_2$, exceeding the 73% rejection observed for the unmodified TFC membrane. This enhancement indicated that dendrimer-treated membranes provided more favorable repulsive interactions, due to increased positive charge and an enhanced Donnan effect [87]. In contrast, the rejection of LiCl decreased to 30% at TFC-Den$_2$ and then increased slightly to 37% at TFC-Den$_3$. The lower rejection of LiCl was consistent with its smaller hydrated radius and weaker interactions with the functional groups on the membrane surface (as supported by DFT calculation), allowing greater permeation. Furthermore, the significantly higher hydration energy of Mg^{2+} ($\Delta H = -1828$ kJ.mol^{-1}) compared to Li^+ ($\Delta H = -474$ kJ.mol^{-1}) created a larger dehydration barrier to membrane transport, which contributed to its greater rejection [5].

In binary-component experiments (Figure 5b), Mg^{2+} rejection increased from 64% in the unmodified TFC to 89% in TFC-Den$_2$, while Li^+ rejection decreased from −25% to −72%, indicating preferential Li^+ permeation. Meanwhile, the flux declined from 44 LMH to 23 LMH due to increased transport resistance associated with the dendrimer layer. The Li^+/Mg^{2+} selectivity increased fourfold from 3.5 in the pristine TFC to 15.6 in TFC-Den$_2$.

To explore the topic beyond Donnan exclusion and the size-exclusion effect, the separation trends were compared with DFT calculations. The experimental findings and trends were consistent with earlier DFT predictions, which supported stronger coordination between dendrimer components and Mg^{2+} ions, particularly through the oxygen-donor groups in the Arg and Lys segments. These segments functioned as localized negatively charged microdomains, creating electrostatic barriers that favored the retention of divalent cations and delayed the permeation of Mg^{2+}. In contrast, Li^+ ions exhibited weaker and more transient interactions with the dendrimer, especially with Lys, facilitating their passage. This behavior was attributed to the ion-adhesion effect [88], which contributed to enhanced membrane selectivity toward Li^+. It was further predicted by the smaller HOMO-LUMO energy gap of Li^+ complexes, indicating lower stability and higher mobility. Taken together with the DFT-predicted coordination trends, the experimental data are consistent with a selective coordination environment that enhances Mg^{2+} rejection while permitting Li^+ passage. This ligand-assisted cation selectivity resembles the interaction-confinement behavior described by Zuo et al. [89], where selective ion retention arose from a combination of confinement and favorable ion-matrix interactions. In our system, immobilized ligands mimicked this mechanism by providing coordination sites that promoted the retention of divalent cations, thereby surpassing the limitations of surface charge effects or size sieving [90]. However, excessive dendrimer loading could interfere with non-specific transport pathways, disrupting localized ion adhesion and ultimately reducing selectivity.

3.4.2 | Influence of Feed Conditions

To evaluate the selectivity of dendrimer-modified membranes, TFC-Den$_2$ was selected as the optimal membrane from those tested. Additional experiments were conducted to assess its separation performance under various binary feed conditions, including variations in feed concentration, the Li^+/Mg^{2+} feed ratio, and feed pH.

Figure 6 presents the experimental results. As shown in Figure 6a, at a fixed total feed concentration of 1000 ppm and varying Li^+/Mg^{2+} mass ratios from 1:1 to 1:100, Mg^{2+} rejection remained relatively stable, fluctuating by approximately 6% from an initial 93% at the 1:1 ratio. In contrast, Li^+ rejection became increasingly negative, dropping from −12% to −93% with increasing Mg^{2+} ratio, reflecting progressively higher Li^+ permeation. Despite these variations, Li^+/Mg^{2+} selectivity remained relatively constant, ranging from 16.0 to a minimum of 14.8. At a higher Mg^{2+} ratio, the divalent cation showed a stronger affinity for dendrimer car-

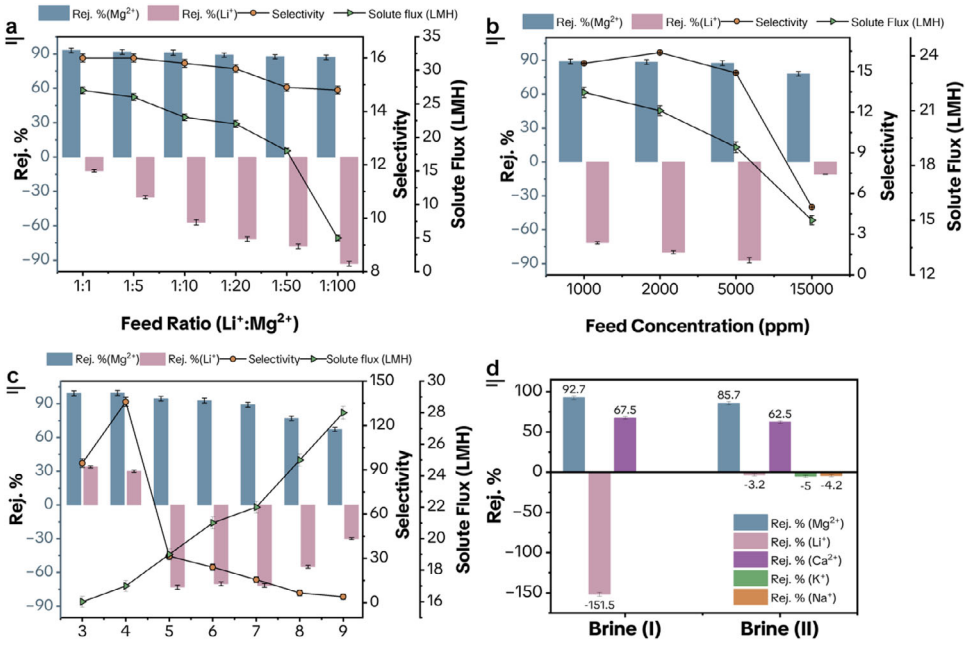

FIGURE 6 | Effect of feed condition on the separation performance of TFC-Den$_2$ membrane. (a) Li^+/Mg^{2+} ratio ranging from (1:1 to 1:100), showing enhanced Li^+ permeation at higher Mg^{2+} ratios, (c) pH (3 to 9), with superior selectivity of 136 observed at pH 4, (b) Total feed concentration, where selectivity declined sharply above 15,000 ppm, and (d) Performance in simulated real brines with varying ionic strength and competing ions. All measurements were conducted in triplicate (n = 3); error bars represent standard deviation.

boxylate groups compared to Li^+, indicating that the interaction with these groups was stronger for Mg^{2+}, consistent with DFT results. Moreover, the transmembrane passage of Cl^- drove co-transport of cations to establish electroneutrality in the permeate. Since Li^+ has a higher diffusion coefficient, it preferentially crossed the membrane, leading to a significant negative rejection value for Li^+ [91, 92].

To provide quantitative support, we estimated the diffusion coefficients (D_i^0, $m^2.S^{-1}$) of Li^+ and Mg^{2+} in aqueous solution using their limiting ionic conductivities via the Nernst-Einstein relation (Equation 1) [93]:

$$D_i^0 = \frac{RT}{|Z_i| F^2} \lambda_i^0 \quad (1)$$

where R is the gas constant (8.314 $J.mol^{-1}.K^{-1}$), T denotes the temperature (298 K), F shows the Faraday constant (96485 $C.mol^{-1}$), Z_i is the ionic charge, and λ_i^0 ($S.m^2.mol^{-1}$) attributes to the limiting molar ionic conductivity. From standard conductivity tables [94], the calculated values ($D_{Li}{}^+ = 1.0 \times 10^{-9}$ m^2 s^{-1} and $D_{Mg}{}^{2+} = 3.5 \times 10^{-10}$ m^2 s^{-1}) indicate that Li^+ has three times higher mobility than Mg^{2+} in aqueous media. In our mixed Mg^{2+} rich feed solution, this suggests that under conditions of strong Mg^{2+} rejection by the membrane, Li^+ is more mobile, which explains the observed significantly negative rejection of Li^+."

At a fixed Li^+/Mg^{2+} mass ratio (1:20), increasing the bulk concentration had a pronounced influence on selectivity (Figure 6b). Li^+/Mg^{2+} selectivity increased slightly to 16.4 at 2,000 ppm, then sharply declined to 5.0 at 15,000 ppm, indicating reduced separation efficiency at high ionic strength. Two coupled phenomena dominate at elevated concentration. First, concentration polarization (CP) thickens the boundary layer and increases the salt concentration at the membrane surface, thereby reducing the transmembrane chemical-potential gradient ($\mu \propto \ln a$, where a is the ion activity) for both ions [95, 96]. The simultaneous rise in osmotic pressure and solution viscosity further depresses permeate flux, thereby reducing the effective driving force and lowering the apparent rejections of Mg^{2+} and Li^+. Second, electric double-layer (EDL) compression ($\kappa^{-1} \propto I^{-1/2}$, where I is the ionic strength) screens the membrane's fixed charge, diminishing Donnan exclusion and amplifying co-ion leakage. Under these conditions, short-range interactions, such as Van der Waals forces, and hindered convection become relatively more important, thereby reducing charge-based selectivity. Interestingly, Li^+ rejection increased significantly at 15 000 ppm to less negative values. Multivalent counterions preferentially occupy/neutralize high-affinity functional groups, narrowing the effective pore free volume. This competitive occupancy impedes Li^+ passage (raising its rejection) while CP and EDL compression simultaneously decrease Mg^{2+} exclusion, yielding a net drop in selectivity [91, 97].

Subsequently, the separation performance of TFC-Den$_2$ was evaluated across a wide pH range (3–9). As shown in Figure 6c, Mg^{2+} rejection was highest under strongly acidic conditions, reaching 99.5% at pH 4 and remaining similarly high at pH 3 (99.3%). Beyond pH 5, Mg^{2+} rejection decreased steadily, reaching around 67% at pH 9. Li^+ followed an opposite trend: at pH 3–4 it showed moderate rejection (33.8% at pH 3 and 30% at pH 4), but shifted sharply to negative rejection at pH 5 (−73%), then gradually increased to approximately −30% at pH 9. Although Li^+ permeation increased with pH, the overall Li^+/Mg^{2+} selectivity decreased, with the maximum value of 136 obtained at pH 4.

TABLE 2 | Estimated degree of protonation of dendrimer functional groups at different pH values.

Group	pKa	pH (Protonation Degree)		
		pH 3 [%]	pH 7 [%]	pH 9 [%]
COOH-(Arg/Lys)	2.2	14	0	0
α-amine (NH_3^+)-(Arg/Lys)	9	100	99	50
ε-amine (NH_3^+)-(Lys)	10.5	100	100	97
Guanidinium-(Arg)	12.5	100	100	100
TAP-ring N	1.3	2	0	0
TAP-exocyclic N	7.1	100	56	1

These trends reflect the protonation-deprotonation behavior of the dendrimer segments, consistent with earlier DFT calculations [98]. At low pH, the amine and guanidinium of Arg and Lys (pKa of 12.5 and 9–10.5) [99–102] remain fully protonated, producing a highly positive interface that strongly excludes Mg^{2+} electrostatically while suppressing metal-ligand coordination. TAP, whose nitrogen sites have pKa values of 1.3 and 7.1 [86, 103], shows limited available donor sites. Together, this extensive protonation minimizes coordination but maximizes Donnan exclusion, leading to high Mg^{2+} rejection and moderate Li^+ passage. As pH increases, progressive deprotonation of Arg, Lys, TAP, and the polyamide carboxyl groups reduces the net positive charge and restores the availability of oxygen and nitrogen-donor sites. The transport mechanism therefore transitions from being dominated by electrostatic exclusion at low pH to increasingly coordination-assisted at higher pH, which weakens Mg^{2+} rejection and enhances Li^+ permeation [86, 103]. In all cases, Mg^{2+} rejection consistently exceeded that of Li^+, consistent with DFT predictions of stronger divalent cation coordination.

Water flux increased progressively from pH 3 to 9. We attribute this to the pH-dependent fixed charge of the dendrimer overlayer: as amine groups (TAP, Lys) partially deprotonate and carboxylates (BTC, NH_2-BDC) deprotonate, the net positive charge diminishes, lowering counter-anions (e.g., Cl^-) partitioning into the selective layer (Donnan/Manning partitioning) [104, 105]. Hence, the intramembrane salt concentration and local osmotic pressure fall. Because water flux follows $J_w = A\ (\Delta P - \Delta\pi_{eff})$, a smaller intrafilm osmotic opposing pressure ($\Delta\pi_{eff}$) yields a higher flux. In fact, the resulting reduction of the internal osmotic penalty increases the effective driving force for water and raises flux. In parallel, the weakened cationic charge at alkaline pH reduces Donnan exclusion of Mg^{2+} (lower Mg^{2+} rejection at pH 8–9) and explains the more negative Li^+ rejection observed near pH 5–7 when the fixed-charge density is highest.

To provide a clearer view of the pH-dependent behavior, we estimated the degree of protonation of the dendrimer functional groups using their literature pKa values (for free amino acids) and the Henderson-Hasselbalch relationship [106]. The degree of protonation (α) was calculated using Equation (2):

$$\alpha = \frac{1}{1 + 10^{(pH - pK_a)}} \quad (2)$$

TABLE 3 | Composition of simulated real brines used for TFC-Den_2 membrane performance evaluation.

Ion	Ion Concentration (ppm)	
	Simulated Brine (I)	Simulated Brine (II)
Li^+	57.2	60.3
Na^+	—	3945.6
K^+	—	1195
Mg^{2+}	1270.5	1472
Ca^{2+}	55.3	57
Cl^-	3582	10700
SO_4^{2-}	51.1	52.5
Total	**5016.1**	**17482.5**

As summarized in Table 2, the amine groups of Arg and Lys remain strongly protonated at pH 3, consistent with the positive zeta potential. In contrast, the carboxylic acid and TAP nitrogen sites become largely deprotonated around pH 7. This shift likely reduces the net surface charge and increases the availability of coordination sites, which helps explain the transition from electrostatic exclusion to coordination-assisted transport at higher pH values.

The applicability of the optimized TFC-Den2 membrane for real-world applications was evaluated by assessing its separation performance in two simulated brine solutions (Figure 6d). Brine (I) contained Mg^{2+}, Li^+, Ca^{2+}, SO_4^{2-}, and Cl^-, with a total concentration of ~5,000 ppm. Brine (II) additionally included interfering cations, Na^+ and K^+, with a total concentration of ~17,500 ppm (Table 3). These compositions were referenced from the Smackover and Clayton Valley brines in the United States [107, 108].

In Brine (I), the TFC-Den_2 membrane achieved high Mg^{2+} rejection (92.5%), followed by lower rejection for Ca^{2+}, attributed to its smaller hydrated radius compared to Mg^{2+}, allowing easier passage. Simultaneously, Li^+ permeation increased significantly, with a negative rejection of −151.5%. The membrane flux decreased from 23 LMH to 19 LMH, and Li^+/Mg^{2+} selectivity improved compared to the binary feed system (reaching 34).

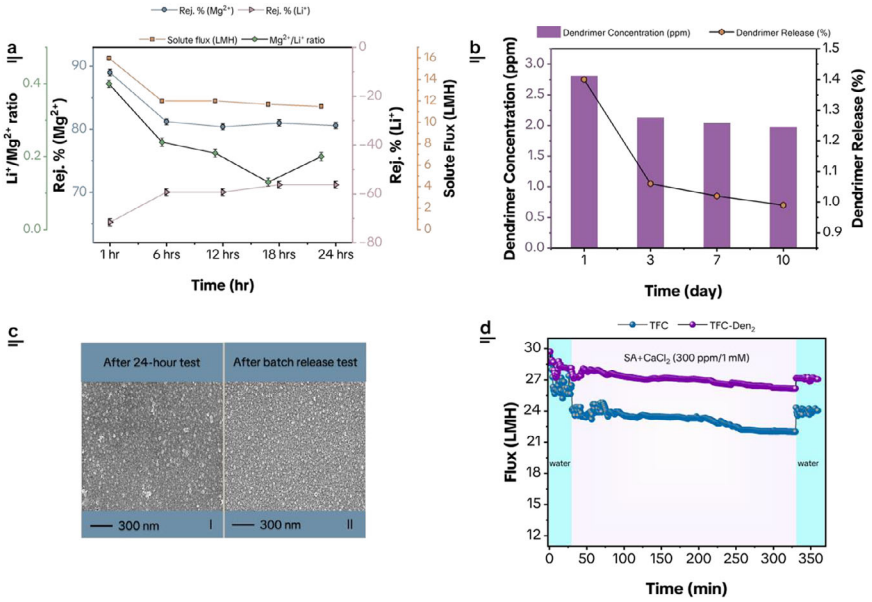

FIGURE 7 | Long-term stability and antifouling performance of TFC-Den_2 membrane. (a) Long-term separation performance in binary salt solution (1000 ppm, Li^+/Mg^{2+} = 1:20, n = 3). (b) Dendrimer batch release over 10 days in DI water (pH 7, 100 rpm shaking), showing less than 0.5% release. (c) Top-surface SEM images after 24 h of dynamic filtration (left) and batch release testing (right). (d) Antifouling performance against SA (300 ppm) and $CaCl_2$ 1 mM.

In contrast, Brine (II) had a higher overall ionic strength and contained interfering monovalent cations (Na^+ and K^+), with hydrated sizes similar to Li^+. In this case, Li^+ rejection became less negative (from −151.5% to −3.2%) due to competition with coexisting monovalent cations, but still indicated continued permeation. This reduced selectivity among monovalent cations was accompanied by a slight decrease in the rejection of Mg^{2+} [22]. Despite these limitations in ion selectivity, the membrane still achieved a flux of 14 LMH and a Li^+/Mg^{2+} selectivity of 8.7. This performance, maintained even under a nearly threefold higher total ion concentration than Brine (I), demonstrated the membrane's applicability in more challenging environments.

3.4.3 | Membrane Long-Term Stability and Antifouling Properties

A common issue with surface-modified TFC membranes is their limited stability. It is essential to maintain the membrane's surface functionality, charge, and ion selectivity over time, as extreme conditions can disrupt the interaction between the surface modifier (the dendrimer) and the TFC membrane. To validate its practical applicability, the TFC-Den_2 membrane was evaluated through a cross-flow filtration process over 24 h using a binary salt solution with a 1,000 ppm concentration (Li^+/Mg^{2+} ratio of 1:20). Key parameters, including Mg^{2+} and Li^+ rejections, flux, and the Li^+/Mg^{2+} ratio, were assessed. The results in Figure 7a indicated the long-term stability of the TFC-Den_2 membrane. During the first 6 h, Mg^{2+} rejection declined slightly (~8%), while Li^+ rejection increased by about 11%. Thereafter, both rejections stabilized, fluctuating within a narrow range (less than 1% for Mg^{2+} and around 3% for Li^+), indicating robust membrane performance. This initial shift was attributed to the detachment of loosely bound dendrimer segments, while the remaining functional groups maintained stability throughout the test. The membrane flux decreased by ~4 LMH in the first 6 h, after which it remained relatively stable. Importantly, the Li^+/Mg^{2+} ratio in the brine increased fourfold, from its initial value of 1:20 (~0.05) to 1:5 (~0.2) during this period. These findings highlighted the potential of the modified TFC-Den_2 membrane for high Li^+ enrichment and long-term brine treatment processes [88].

Furthermore, the long-term stability of the dendrimer-modified membrane was evaluated via a 10-day release test in aqueous solution at pH 7 (Figure 7b). The initial dendrimer concentration in the solution was approximately 2.81 ppm. A slight initial release (~0.15%) occurred within the first 3 days, due to the desorption of weakly attached dendrimer segments. After this phase, the dendrimer concentration gradually declined to 1.97 ppm by day 10 (~0.4% total release). The release profile stabilized over the remaining 7 days, fluctuating minimally. These results strengthen the evidence that dendrimers were firmly anchored to the membrane surface, ensuring stability in neutral conditions.

We note that there are various interactions between the dendrimer and the membrane surface, including hydrogen bonds, van der Waals forces, electrostatic forces, and hydrophobic interactions. These interactions directly influence the release of the dendrimer. Dendrimer segments that are attached through electrostatic interactions are likely to be released during the initial burst release phase [109, 110]. It is important to note that feed conditions can influence dendrimer release. Higher salinity can result in salts binding to zwitterionic functional groups, which screens electrostatic interactions and forms transient ion pairs, which typically do not lead to measurable material loss [111–114]. In contrast, strongly acidic conditions can induce greater release because higher protonation of the amine groups in dendrimers reduces both electrostatic interactions and hydrogen bonding, thereby increasing desorption [115, 116].

TABLE 4 | Comparison of the performance of the TFC-Den_2 membrane with previously reported membranes for Li^+/Mg^{2+} separation in the binary $LiCl/MgCl_2$ feed solution.

NF Membrane Modifier	Li^+: Mg^{2+} Feed Ratios	Rejection (%)		Permeability (LMHB)	SF (Li^+, Mg^{2+})	Refs.
		Mg^{2+}	Li^+			
NF90	1:20	60.5	15	9.78	2.1	[120]
NF270	1:30	79	10.5	_	3.03	[121]
PEI[a]	1:30	96.11	21.76	4.17	12.15	[19]
BPEI-EDTA[b]	1:24	>91	~30	0.6	9.2	[122]
PEI-LS[c]	1:20	80	6	14.5	4.7	[20]
PHF[d]	1:21	92	−10	6.7	13.1	[13]
PEI-γ-CDs[e]	_	~96	~61	4.86	10.8	[24]
PEI-AAN[f]	1:20	99.28	60.38	8.9	53.9	[123]
PEI-DTES[g]	1:20	91.64	−10.5	6.2	12.95	[124]
TbTG-COF[h]	1:20	99	~19	7.9	73	[125]
TFC-Den_2	1:20	89	−72	7.25	15.6	This work

[a]PEI: Polyethyleneimine.
[b]BPEI-EDTA: Branched polyethyleneimine-Ethylenediamine tetraacetic acid.
[c]LS: Lignosulfonate.
[d]PHF: Branched polyethyleneimine.
[e]γ-CD: γ-Cyclodextrin.
[f]AAN: Aminoacetonitrile.
[g]DTES: 3-Diamino-methyl-cyclohexyl triethoxysilane.
[h]TbTG-COF: Guanidinium covalent organic framework (TbTG nanosheets).

SEM was used to observe the TFC-Den_2 membrane after 10 days of immersion in water with vigorous shaking, and following a 24-h dynamic stability test, to evaluate stability under realistic filtration conditions. The results in Figure 7c indicate that the membrane retained its structural integrity compared with the intact TFC-Den_2 image shown in Figure 3a. During the stability test, the membrane exhibited only slight surface smoothing in the binary salt solution, likely due to the shear stress imposed by the dynamic cross-flow test conditions. Additionally, the release test confirmed that the membrane surface remained intact, with no significant leaching of the dendrimers. Taken together, the long-term stability results suggest that the surface-bound dendrimer maintains compatibility with the polyamide layer without introducing mechanical rigidity or loss of flexibility.

The antifouling performance of both unmodified TFC and TFC-Den_2 membranes was assessed through a continuous 6-h fouling test (Figure 7d) using SA and calcium ions (Ca^{2+}) as the model organic foulant system. The pristine TFC membrane exhibited a more substantial flux decline, with a steeper and continuous drop resulting in an FDR of 15.3%. In contrast, the TFC-Den_2 membrane showed significantly improved fouling resistance, with a much milder FDR of only 6.5%. After a simple 20-min rinse with DI water, the TFC-Den_2 membrane recovered 96.6% of its initial flux, whereas the pristine TFC recovered 92%. This improvement is attributed to the hydrophilic dendrimer layer, which promotes the formation of a hydration layer of water molecules on the membrane surface, thereby increasing surface resistance to foulant adhesion. Additionally, the increased surface charge of TFC-Den_2 likely reduced Ca^{2+} adsorption through Donnan exclusion, minimizing calcium-mediated bridging with alginate [25]. This hypothesis proposes that alginate, which contains COO^-, can coordinate with metal cations such as Ca^{2+}. This coordination can cross-link adjacent chains, forming a cross-linked film and thereby intensifying fouling [117–119].

3.5 | Comparison with Other Studies

Table 4 compares the performance of the TFC-Den_2 membrane with other reported membranes developed for Li^+/Mg^{2+} separation. While some membranes achieved higher Mg^{2+} rejection, they had poor Li^+ permeation and limited separation selectivity. Additionally, many high-rejection membranes suffered from significantly reduced permeate flux, which limited their practical applicability. In contrast, the TFC-Den_2 membrane demonstrated a well-balanced performance across key parameters, including flux, ion rejection, and selectivity, highlighting its strong potential for efficient lithium recovery from magnesium-rich brines. Notably, several of the compared studies did not investigate antifouling behavior, overlooking a critical aspect of real-world performance.

By coupling pH-tunable coordination chemistry with a chemically stable dendrimer interface, the TFC-Den_2 membrane delivers high separation efficiency together with operational robustness, offering a more comprehensive and application-relevant solution than existing NF or TFN systems.

4 | Conclusions

We developed a polypeptide dendrimer-modified TFC membrane (TFC-Den) that introduces a zwitterionic, pH-tunable coordination interface for selective lithium enrichment. The membrane maintained strong Mg^{2+} rejection while enabling high Li^{+} recovery across different feed compositions, achieving a selectivity of 136 at pH 4 and maintaining effective separation at neutral pH. These trends are consistent with DFT-calculated binding preferences, which indicate stronger interactions with Mg^{2+}, particularly for lysine-based coordination sites, clarifying the coordination-regulated transport mechanism that extends beyond simple Donnan exclusion. The TFC-Den membrane also performed well in simulated real brine, enriching Li^{+} by over 150%, and exhibited good operational stability with a low flux-decline ratio (6.5%). Nonetheless, further studies are needed to evaluate performance under higher salinities, battery-leachate streams, long-term chemical stability under acidic conditions, and biologically relevant conditions. The separation of Li^{+} from Na^{+} also remains a key challenge due to their similar ionic characteristics.

This work demonstrates a coordination-driven strategy that combines DFT-guided molecular design, bioinspired functionalization, and interfacial membrane engineering for selective lithium recovery from high-salinity brines. This approach provides a framework for designing next-generation coordination-based membranes for resource recovery applications.

Acknowledgements

The financial support for this work, provided by Alberta Innovates, the Natural Sciences and Engineering Research Council of Canada, and Canada's Oil Sands Innovation Alliance (COSIA), is gratefully acknowledged.

Conflicts of Interest

The authors declare no conflict of interest.

Data Availability Statement

The data that support the findings of this study are available from the corresponding author upon reasonable request.

References

1. H. Yu, H. Yang, K. Chen, et al., "Non–Closed–Loop Recycling Strategies for Spent Lithium–Ion Batteries: Current Status and Future Prospects," *Energy Storage Materials* 67 (2024): 103288, https://doi.org/10.1016/j.ensm.2024.103288.

2. M. L. Vera, W. R. Torres, C. I. Galli, A. Chagnes, and V. Flexer, "Environmental Impact of Direct Lithium Extraction from Brines," *Nature Reviews Earth & Environment* 4 (2023): 149–165, https://doi.org/10.1038/s43017-022-00387-5.

3. J. J. Roy, S. Rarotra, V. Krikstolaityte, et al., "Green Recycling Methods to Treat Lithium-Ion Batteries E-Waste: A Circular Approach to Sustainability," *Advanced Materials* 34 (2022): 2103346, https://doi.org/10.1002/adma.202103346.

4. T. Zhang, W. Zheng, Q. Wang, Z. Wu, and Z. Wang, "Designed Strategies of Nanofiltration Technology for Mg2+/Li+ Separation from Salt-Lake Brine: A Comprehensive Review," *Desalination* 546 (2023): 116205, https://doi.org/10.1016/j.desal.2022.116205.

5. Y. Guo, Y. Ying, Y. Mao, X. Peng, and B. Chen, "Polystyrene Sulfonate Threaded through a Metal–Organic Framework Membrane for Fast and Selective Lithium-Ion Separation," *Angewandte Chemie* 128 (2016): 15344–15348, https://doi.org/10.1002/ange.201607329.

6. F. Soyekwo, H. Wen, D. Liao, and C. Liu, "Fouling-Resistant Ionic Graft-Polyamide Nanofiltration Membrane with Improved Permeance for Lithium Separation from MgCl2/LiCl Mixtures," *Journal of Membrane Science* 659 (2022): 120773, https://doi.org/10.1016/j.memsci.2022.120773.

7. M. Kumar, M. A. Khan, and H. A. Arafat, "Recent Developments in the Rational Fabrication of Thin Film Nanocomposite Membranes for Water Purification and Desalination," *ACS Omega* 5 (2020): 3792–3800, https://doi.org/10.1021/acsomega.9b03975.

8. F. Soyekwo, H. Wen, D. Liao, and C. Liu, "Nanofiltration Membranes Modified with a Clustered Multiquaternary Ammonium-Based Ionic Liquid for Improved Magnesium/Lithium Separation," *ACS Applied Materials & Interfaces* 14 (2022): 32420–32432, https://doi.org/10.1021/acsami.2c03650.

9. S. J. Lounder and A. Asatekin, "Zwitterionic Ion-Selective Membranes with Tunable Subnanometer Pores and Excellent Fouling Resistance," *Chemistry of Materials* 33 (2021): 4408–4416, https://doi.org/10.1021/acs.chemmater.1c00374.

10. S. Yang, Y. Wang, H. Pan, P. He, and H. Zhou, "Lithium Extraction from Low-Quality Brines," *Nature* 636 (2024): 309–321, https://doi.org/10.1038/s41586-024-08117-1.

11. S. Divakar, M. Padaki, and R. G. Balakrishna, "Review on Liquid–Liquid Separation by Membrane Filtration," *ACS Omega* 7 (2022): 44495–44506, https://doi.org/10.1021/acsomega.2c02885.

12. Y. Liang, Y. Zhu, C. Liu, et al., "Polyamide Nanofiltration Membrane with Highly Uniform Sub-Nanometre Pores for Sub-1 Å Precision Separation," *Nature Communications* 11 (2020): 2015.

13. Q. Shen, S. J. Xu, Z. L. Xu, H. Z. Zhang, and Z. Q. Dong, "Novel Thin-Film Nanocomposite Membrane with Water-Soluble Polyhydroxylated Fullerene for the Separation of Mg 2+ /Li + Aqueous Solution," *Journal of Applied Polymer Science* 136 (2019): 48029, https://doi.org/10.1002/app.48029.

14. S. Guo, X. Yan, Z. Luo, J. Zhang, and C. Yuan, "Preparation of Positively Charged Nanofiltration Membranes: Manipulation of the Positive Charge," *Desalination* 586 (2024): 117780, https://doi.org/10.1016/j.desal.2024.117780.

15. B. Yuan, N. Wang, S. Zhao, et al., "Polyamide Nanofiltration Membrane Fine-Tuned via Mixed Matrix Ultrafiltration Support to Maximize the Sieving Selectivity of Li+/Mg2+ and Cl–/SO42–," *Desalination* 538 (2022): 115929, https://doi.org/10.1016/j.desal.2022.115929.

16. J. Hou, H. Zhang, A. W. Thornton, A. J. Hill, H. Wang, and K. Konstas, "Lithium Extraction by Emerging Metal–Organic Framework-Based Membranes," *Advanced Functional Materials* 31 (2021): 2105991, https://doi.org/10.1002/adfm.202105991.

17. H. Peng and Q. Zhao, "A Nano-Heterogeneous Membrane for Efficient Separation of Lithium from High Magnesium/Lithium Ratio Brine," *Advanced Functional Materials* 31 (2021): 2009430, https://doi.org/10.1002/adfm.202009430.

18. K. Chen, F. Li, T. Wei, et al., "An Interlayer-Based Positive Charge Compensation Strategy for the Preparation of Highly Selective Mg2+/Li+ Separation Nanofiltration Membranes," *Journal of Membrane Science* 684 (2023): 121882, https://doi.org/10.1016/j.memsci.2023.121882.

19. P. Xu, W. Wang, X. Qian, et al., "Positive Charged PEI-TMC Composite Nanofiltration Membrane for Separation of Li+ and Mg2+ from Brine with High Mg2+/Li+ Ratio," *Desalination* 449 (2019): 57–68, https://doi.org/10.1016/j.desal.2018.10.019.

20. M. Yassari, P. Karami, A. Taghipour, A. Rahimpour, and M. Sadrzadeh, "Sustainable Layer-by-Layer Assembled Nanofiltration Membranes with Optimized Pore Size for Lithium-Magnesium Selective Separation," *Journal of Environmental Chemical Engineering* 13 (2025): 116478, https://doi.org/10.1016/j.jece.2025.116478.

21. Z. Yang, W. Fang, Z. Wang, R. Zhang, Y. Zhu, and J. Jin, "Dual-Skin Layer Nanofiltration Membranes for Highly Selective Li+/Mg2+ Separation," *Journal of Membrane Science* 620 (2021): 118862, https://doi.org/10.1016/j.memsci.2020.118862.

22. A. Aghaei, M. A. Islam, E. Jashni, A. Khalili, J. Y. Cho, and M. Sadrzadeh, "Efficient Lithium Recovery from Water Using Polyamide Thin-Film Nanocomposite (TFN) Membrane Modified with Positively Charged Silica Nanoparticles," *ACS Applied Materials & Interfaces* 16 (2024): 66514–66531, https://doi.org/10.1021/acsami.4c15939.

23. Y. Feng, H. Peng, and Q. Zhao, "Fabrication of High Performance Mg2+/Li+ Nanofiltration Membranes by Surface Grafting of Quaternized Bipyridine," *Separation and Purification Technology* 280 (2022): 119848, https://doi.org/10.1016/j.seppur.2021.119848.

24. Y. Zhao, N. Li, J. Shi, et al., "Extra-Thin Composite Nanofiltration Membranes Tuned by γ-Cyclodextrins Containing Amphipathic Cavities for Efficient Separation of Magnesium/Lithium Ions," *Separation and Purification Technology* 286 (2022): 120419, https://doi.org/10.1016/j.seppur.2021.120419.

25. D. Lu, T. Ma, S. Lin, et al., "Constructing a Selective Blocked-Nanolayer on Nanofiltration Membrane via Surface-Charge Inversion for Promoting Li+ Permselectivity over Mg2+," *Journal of Membrane Science* 635 (2021): 119504, https://doi.org/10.1016/j.memsci.2021.119504.

26. S. Karan, Z. Jiang, and A. G. Livingston, "Sub–10 Nm Polyamide Nanofilms with Ultrafast Solvent Transport for Molecular Separation," *Science* 348 (2015): 1347–1351.

27. L. Cao, I. C. Chen, Z. Li, et al., "Switchable Na+ and K+ Selectivity in an Amino Acid Functionalized 2D Covalent Organic Framework Membrane," *Nature Communications* 13 (2022): 7894.

28. I. Sadeghi, J. Kronenberg, and A. Asatekin, "Selective Transport through Membranes with Charged Nanochannels Formed by Scalable Self-Assembly of Random Copolymer Micelles," *ACS Nano* 12 (2018): 95–108, https://doi.org/10.1021/acsnano.7b07596.

29. Z. Lu, Y. Wu, L. Ding, Y. Wei, and H. Wang, "A Lamellar MXene (Ti 3 C 2 T x)/PSS Composite Membrane for Fast and Selective Lithium-Ion Separation," *Angewandte Chemie International Edition* 60 (2021): 22265–22269, https://doi.org/10.1002/anie.202108801.

30. T. Xu, B. Wu, L. Hou, et al., "Highly Ion-Permselective Porous Organic Cage Membranes with Hierarchical Channels," *Journal of the American Chemical Society* 144 (2022): 10220–10229, https://doi.org/10.1021/jacs.2c00318.

31. Y. Zhang, Z. Hao, I. Hussein, Z. Wang, and S. Zhao, "Tunable Ionic Sieving Membrane via Reactive Layer-by-Layer Assembly of Porous Organic Cages," *Advanced Functional Materials* 34 (2024): 2315750, https://doi.org/10.1002/adfm.202315750.

32. H. Wang, Y. Zhai, Y. Li, et al., "Covalent Organic Framework Membranes for Efficient Separation of Monovalent Cations," *Nature Communications* 13 (2022): 7123.

33. Y. Lv, Z. Dai, Y. Chen, et al., "Two-Dimensional Sulfonate-Functionalized Metal–Organic Framework Membranes for Efficient Lithium-Ion Sieving," *Nano Letters* 24 (2024): 2782–2788, https://doi.org/10.1021/acs.nanolett.3c04773.

34. N. Li, F. Chen, J. Shen, et al., "Buckyball-Based Spherical Display of Crown Ethers for De Novo Custom Design of Ion Transport Selectivity," *Journal of the American Chemical Society* 142 (2020): 21082–21090, https://doi.org/10.1021/jacs.0c09655.

35. N. Gan, Y. Lin, B. Wu, et al., "Supramolecular-Coordinated Nanofiltration Membranes with Quaternary-Ammonium Cyclen for Efficient Lithium Extraction from High Magnesium/Lithium Ratio Brine," *Water Research* 268 (2025): 122703, https://doi.org/10.1016/j.watres.2024.122703.

36. R. Xu, Y. Kang, W. Zhang, B. Pan, and X. Zhang, "Two-Dimensional MXene Membranes with Biomimetic Sub-Nanochannels for Enhanced Cation Sieving," *Nature Communications* 14 (2023): 4907.

37. B. Han, Y. Sim, Q. Yan, N. Mathews, and J. C. P. Gabriel, "From Electronic Wastes to Efficient and Specific Filtration Membranes: A Photovoltaic Upcycling Case Enabling Silver Urban Mining," *Journal of Cleaner Production* 505 (2025): 145528, https://doi.org/10.1016/j.jclepro.2025.145528.

38. B. Han, Z. Liu, D. Xia, G. Zante, Q. Yan, and J. C. P. Gabriel, "Enhanced Silver Recovery from Electronic Wastes Using Ionic Liquid-Integrated Nanocomposite Membrane," *Separation and Purification Technology* 366 (2025): 132689, https://doi.org/10.1016/j.seppur.2025.132689.

39. B. Kanlayaprasit, J. Park, Y. Lee, and T.-H. Bae, "Amine-Functionalized Zirconium–Ellagate Framework for Enhanced Water Permeance and Ion Selectivity in Thin-Film Nanocomposite Nanofiltration Membranes," *Journal of Water Process Engineering* 80 (2025): 109154, https://doi.org/10.1016/j.jwpe.2025.109154.

40. P. Cheng, T. Chen, T. Liu, et al., "Covalent/Metal–Organic Framework Membranes with Tailored Pore Functionality for Accurate Ion Separation," *Chemical Science* 16 (2025): 22900–22932.

41. Y. Du, D. Lei, X. Hao, Z. Liu, and X. Du, "Crown Ether-Functionalized 3D COF Membrane with Ion-Recognition Sites for Enhanced Monovalent Cation Selectivity," *Separation and Purification Technology* 376 (2025): 133979, https://doi.org/10.1016/j.seppur.2025.133979.

42. C. Jiang, S. Bai, J. Li, M. Wang, Y. Zhou, and Y. Hou, "Crown Ether-Functionalized Nanofiltration Membranes with High Ions Selectivity for Li+/Mg2+ Separation," *Journal of Membrane Science* 714 (2025): 123372, https://doi.org/10.1016/j.memsci.2024.123372.

43. S. Niazkhani, F. Aminsharei, S. A. Hassanzadeh-Tabrizi, A. Malekzadeh, and E. Ameri, "Synthesis and Modification of Nanofiltration Membranes with Dendrimer-Modified Graphene Oxide to Remove Lead and Cadmium Ions from Aqueous Solutions," *Cleaner Engineering and Technology* 23 (2024): 100843, https://doi.org/10.1016/j.clet.2024.100843.

44. H. Ranjbaran, E. Ameri, and B. Dehghani, "Preparation of Dendrimer/TiO2 Polysulfone Nanofiltration Membrane to Improve Antibacterial, Antifouling and Separation Performance of Contaminants (heavy metals, salts, dyes)," *Polymer Bulletin* 81 (2024): 1471–1494, https://doi.org/10.1007/s00289-023-04785-7.

45. A. M. Saenz De Jubera, Y. Gao, J. S. Moore, D. G. Cahill, and B. J. Mariñas, "Enhancing the Performance of Nanofiltration Membranes by Modifying the Active Layer with Aramide Dendrimers," *Environmental Science & Technology* 46 (2012): 9592–9599, https://doi.org/10.1021/es301392w.

46. A. M. Saenz De Jubera, J. H. Herbison, Y. Komaki, et al., "Development and Performance Characterization of a Polyamide Nanofiltration Membrane Modified with Covalently Bonded Aramide Dendrimers," *Environmental Science & Technology* 47 (2013): 8642–8649.

47. Y. Gao, A. M. S. De Jubera, B. J. Mariñas, and J. S. Moore, "Nanofiltration Membranes with Modified Active Layer Using Aromatic Polyamide Dendrimers," *Advanced Functional Materials* 23 (2013): 598–607, https://doi.org/10.1002/adfm.201201004.

48. N. Joseph, J. Thomas, P. Ahmadiannamini, et al., "Ultrathin Single Bilayer Separation Membranes Based on Hyperbranched Sulfonated Poly(aryleneoxindole)," *Advanced Functional Materials* 27 (2017): 1605068, https://doi.org/10.1002/adfm.201605068.

49. M. F. Bush, J. T. O'Brien, J. S. Prell, R. J. Saykally, and E. R. Williams, "Infrared Spectroscopy of Cationized Arginine in the Gas Phase: Direct Evidence for the Transition from Nonzwitterionic to Zwitterionic Structure," *Journal of the American Chemical Society* 129 (2007): 1612–1622, https://doi.org/10.1021/ja066335j.

50. M. J. Harms, J. L. Schlessman, M. S. Chimenti, et al., "A Buried Lysine That Titrates with a Normal p K a: Role of Conformational Flexibility at

the Protein–Water Interface as a Determinant of p K a Values," *Protein Science* 17 (2008): 833–845, https://doi.org/10.1110/ps.073397708.

51. M. J. Harms, J. L. Schlessman, G. R. Sue, and E. B. García-Moreno, "Arginine Residues at Internal Positions in a Protein Are Always Charged," *Proceedings of the National Academy of Sciences* 108 (2011): 18954–18959, https://doi.org/10.1073/pnas.1104808108.

52. L. Li, I. Vorobyov, and T. W. Allen, "The Different Interactions of Lysine and Arginine Side Chains with Lipid Membranes," *The Journal of Physical Chemistry B* 117 (2013): 11906–11920, https://doi.org/10.1021/jp405418y.

53. E. Flood, C. Boiteux, and T. W. Allen, "Selective Ion Permeation Involves Complexation with Carboxylates and Lysine in a Model human Sodium Channel," *PLOS Computational Biology* 14 (2018): 1006398, https://doi.org/10.1371/journal.pcbi.1006398.

54. C. T. Armstrong, P. E. Mason, J. L. R. Anderson, and C. E. Dempsey, "Arginine Side Chain Interactions and the Role of Arginine as a Gating Charge Carrier in Voltage Sensitive Ion Channels," *Scientific Reports* 6 (2016): 21759.

55. J. R. Fromm, R. E. Hileman, E. E. O. Caldwell, J. M. Weiler, and R. J. Linhardt, "Differences in the Interaction of Heparin with Arginine and Lysine and the Importance of these Basic Amino Acids in the Binding of Heparin to Acidic Fibroblast Growth Factor," *Archives of Biochemistry and Biophysics* 323 (1995): 279–287, https://doi.org/10.1006/abbi.1995.9963.

56. F. Baskoro, P. C. Chiang, Y. C. Lu, et al., "Columnar Liquid-Crystalline Triazine-Based Dendrimer with Carbon Nanotube Filler for Efficient Organic Lithium-Ion Batteries," *Electrochimica Acta* 434 (2022): 141306, https://doi.org/10.1016/j.electacta.2022.141306.

57. M. Mohana, P. Thomas Muthiah, C. D. Mcmillen, R. J. Butcher, and E. Y. Cheung, "Supramolecular Interactions in Salts/Cocrystals Involving Pyrimidine Derivatives of Sulfonate/Carboxylic Acid," *Acta Crystallographica Section C Structural Chemistry* 79 (2023): 61–67, https://doi.org/10.1107/S2053229623000177.

58. M. Sangavi, M. Mohana, and R. J. Butcher, "Supramolecular Assembly and Structural Insights of 2, 4, 6-triaminopyrimidinium Bis (3, 5-dinitrosalicylato) Diaquamagnesate (II) Dihydrate," *Journal of Chemical Crystallography* 55 (2025): 251–258.

59. B. Németh, C. Wéber, T. Veszprémi, T. Gáti, and Á. Demeter, "Carbon Protonation of 2, 4, 6-triaminopyrimidines: Synthesis, NMR Studies, and Theoretical Calculations," *Journal of Organic Chemistry* 71 (2006): 4910–4918.

60. M. Tagliazucchi, O. Peleg, M. Kröger, Y. Rabin, and I. Szleifer, "Effect of Charge, Hydrophobicity, and Sequence of Nucleoporins on the Translocation of Model Particles through the Nuclear Pore Complex," *Proceedings of the National Academy of Sciences* 110 (2013): 3363–3368, https://doi.org/10.1073/pnas.1212909110.

61. D. Lemoine, R. Jiang, A. Taly, T. Chataigneau, A. Specht, and T. Grutter, "Ligand-Gated Ion Channels: New Insights into Neurological Disorders and Ligand Recognition," *Chemical Reviews* 112 (2012): 6285–6318, https://doi.org/10.1021/cr3000829.

62. W. Shi, J. Shen, L. Shen, et al., "Electrolyte Membranes with Biomimetic Lithium-Ion Channels," *Nano Letters* 20 (2020): 5435–5442, https://doi.org/10.1021/acs.nanolett.0c01910.

63. B. Foucaud, P. Perret, T. Grutter, and M. Goeldner, "Cysteine Mutants as Chemical Sensors for Ligand–Receptor Interactions," *Trends in Pharmacological Sciences* 22 (2001): 170–173, https://doi.org/10.1016/S0165-6147(00)01674-6.

64. Y. Hou, C. Zhu, H. Sun, et al., "Artificial Cation–Chloride Co-Transporters for Chloride-Facilitated Lithium/Magnesium Separation," *Angewandte Chemie International Edition* 64 (2025): 202504259, https://doi.org/10.1002/anie.202504259.

65. S. J. Angyal and W. K. Warburton, "549. The Basic Strengths of Methylated Guanidines," *Journal of the Chemical Society (Resumed)* 1951 (1951): 2492–2494, https://doi.org/10.1039/jr9510002492.

66. S. Hirose, M. Okada, S. Kaneko, and A. Mitsudome, "Are Some Idiopathic Epilepsies Disorders of Ion Channels?: A Working Hypothesis," *Epilepsy Research* 41 (2000): 191–204, https://doi.org/10.1016/S0920-1211(00)00141-8.

67. J. Yang, P. T. Elllnor, W. A. Sather, J. F. Zhang, and R. W. Tsien, "Molecular Determinants of Ca2+ Selectivity and Ion Permeation in L-Type Ca2+ Channels," *Nature* 366 (1993): 158–161, https://doi.org/10.1038/366158a0.

68. D. Yan, H. H. Kristoffersen, J. K. Pedersen, and J. Rossmeisl, "Rationally Tailoring Catalysts for the CO Oxidation Reaction by Using DFT Calculations," *ACS Catalysis* 12 (2022): 116–125, https://doi.org/10.1021/acscatal.1c04331.

69. H. Li, X. Miao, J. Zhang, et al., "DFT Studies on the Reaction Mechanism and Kinetics of Dibutyl Phthalate Initiated by Hydroxyl and Sulfate Radicals: Prediction of the Most Reactive Sites," *Chemical Engineering Journal* 381 (2020): 122680, https://doi.org/10.1016/j.cej.2019.122680.

70. Z. Pan, Y. Lei, F. Zheng, J. Zhan, and G. Han, "Rational Construction of Positively Charged Polyamide Nanofiltration Membranes for Precision Cation Separations," *Journal of Membrane Science* 711 (2024): 123172, https://doi.org/10.1016/j.memsci.2024.123172.

71. S. Mokhtari, A. Rahimpour, A. A. Shamsabadi, S. Habibzadeh, and M. Soroush, "Enhancing Performance and Surface Antifouling Properties of Polysulfone Ultrafiltration Membranes with Salicylate-Alumoxane Nanoparticles," *Applied Surface Science* 393 (2017): 93–102, https://doi.org/10.1016/j.apsusc.2016.10.005.

72. A. Rahimpour, S. F. Seyedpour, S. Aghapour Aktij, et al., "Simultaneous Improvement of Antimicrobial, Antifouling, and Transport Properties of Forward Osmosis Membranes with Immobilized Highly-Compatible Polyrhodanine Nanoparticles," *Environmental Science & Technology* 52 (2018): 5246–5258, https://doi.org/10.1021/acs.est.8b00804.

73. S. Grimme, J. Antony, S. Ehrlich, and H. Krieg, "A Consistent and Accurate Ab Initio Parametrization of Density Functional Dispersion Correction (DFT-D) for the 94 Elements H-Pu," *The Journal of Chemical Physics* 132 (2010): 43, https://doi.org/10.1063/1.3382344.

74. F. Neese, "The SHARK Integral Generation and Digestion System," *Journal of Computational Chemistry* 44 (2023): 381–396, https://doi.org/10.1002/jcc.26942.

75. F. Neese, "Software Update: The ORCA Program System—Version 6.0," *WIREs Computational Molecular Science* 15 (2025): 70019, https://doi.org/10.1002/wcms.70019.

76. S. Grimme, S. Ehrlich, and L. Goerigk, "Effect of the Damping Function in Dispersion Corrected Density Functional Theory," *Journal of Computational Chemistry* 32 (2011): 1456–1465, https://doi.org/10.1002/jcc.21759.

77. A. D. Becke, "Density-Functional Thermochemistry. I. The Effect of the Exchange-Only Gradient Correction," *The Journal of Chemical Physics* 96 (1992): 2155–2160, https://doi.org/10.1063/1.462066.

78. F. Weigend, "Accurate Coulomb-Fitting Basis Sets for H to Rn," *Physical Chemistry Chemical Physics* 8 (2006): 1057, https://doi.org/10.1039/b515623h.

79. G. L. Stoychev, A. A. Auer, and F. Neese, "Automatic Generation of Auxiliary Basis Sets," *Journal of Chemical Theory and Computation* 13 (2017): 554–562, https://doi.org/10.1021/acs.jctc.6b01041.

80. C. Lee, W. Yang, and R. G. Parr, "Development of the Colle-Salvetti Correlation-Energy Formula into a Functional of the Electron Density," *Physical Review B* 37 (1988): 785–789, https://doi.org/10.1103/PhysRevB.37.785.

81. M. D. Hanwell, D. E. Curtis, D. C. Lonie, T. Vandermeerschd, E. Zurek, and G. R. Hutchison, "Avogadro: An Advanced Semantic Chemical Editor, Visualization, and Analysis Platform," *Journal of Cheminformatics* 4 (2012): 17.

82. T. Lu and F. Chen, "Multiwfn: A Multifunctional Wavefunction Analyzer," *Journal of Computational Chemistry* 33 (2012): 580–592, https://doi.org/10.1002/jcc.22885.

83. G. Wolansky and A. Marmur, "Apparent Contact Angles on Rough Surfaces: The Wenzel Equation Revisited," *Colloids and Surfaces A: Physicochemical and Engineering Aspects* 156 (1999): 381–388, https://doi.org/10.1016/S0927-7757(99)00098-9.

84. R. F. Egerton, M. Hayashida, and M. Malac, "Transmission Electron Microscopy of Thick Polymer and Biological Specimens," *Micron* 169 (2023): 103449.

85. A. Radhi, E. Du, and F. Khazaal, "HOMO-LUMO Energies and Geometrical Structures Effecton Corrosion Inhibition for Organic Compounds Predict by DFT and PM3 Methods," *NeuroQuantology* 18 (2020): 37–45.

86. R. S. Balaban, L. J. Mandel, and D. J. Benos, "On the Cross-Reactivity of Amiloride and 2,4,6 Triaminopyrimidine (TAP) for the Cellular Entry and Tight Junctional Cation Permeation Pathways in Epithelia," *The Journal of Membrane Biology* 49 (1979): 363–390, https://doi.org/10.1007/BF01868992.

87. T. Gu, R. Zhang, S. Zhang, et al., "Quaternary Ammonium Engineered Polyamide Membrane with High Positive Charge Density for Efficient Li+/Mg2+Separation," *Journal of Membrane Science* 659 (2022): 120802, https://doi.org/10.1016/j.memsci.2022.120802.

88. W. Ji, Y. Li, F. Duan, et al., "Maintaining High Magnesium/Lithium Selectivity in Nanofiltration at High Salinity: Optimizing Membrane Charge Distribution for Synergistic Donnan and Ion Adhesion Effects," *Journal of Membrane Science* 729 (2025): 124160, https://doi.org/10.1016/j.memsci.2025.124160.

89. P. Zuo, J. Ran, C. Ye, X. Li, T. Xu, and Z. Yang, "Advancing Ion Selective Membranes with Micropore Ion Channels in the Interaction Confinement Regime," *ACS Nano* 18 (2024): 6016–6027, https://doi.org/10.1021/acsnano.3c12616.

90. S. Goutham, A. Keerthi, A. Ismail, et al., "Beyond Steric Selectivity of Ions Using ångström-Scale Capillaries," *Nature Nanotechnology* 18 (2023): 596–601, https://doi.org/10.1038/s41565-023-01337-y.

91. R. He, C. Dong, S. Xu, C. Liu, S. Zhao, and T. He, "Unprecedented Mg2+/Li+ Separation Using Layer-by-Layer Based Nanofiltration Hollow Fiber Membranes," *Desalination* 525 (2022): 115492, https://doi.org/10.1016/j.desal.2021.115492.

92. H. Wu, Y. Lin, W. Feng, et al., "A Novel Nanofiltration Membrane with [MimAP][Tf2N] Ionic Liquid for Utilization of Lithium from Brines with High Mg2+/Li+ Ratio," *Journal of Membrane Science* 603 (2020): 117997, https://doi.org/10.1016/j.memsci.2020.117997.

93. G. H. Gao, H. B. Shi, and Y. X. Yu, "Mutual Diffusion Coefficients of Concentrated 1:1 Electrolyte from the Modified Mean Spherical Approximation," *Fluid Phase Equilibria* 256 (2007): 105–111, https://doi.org/10.1016/j.fluid.2006.11.017.

94. R. A. Robinson and R. H. Stokes, *Electrolyte solutions*, (Courier Corporation, 2002).

95. S. Y. Sun, L. J. Cai, X. Y. Nie, X. Song, and J. G. Yu, "Separation of Magnesium and Lithium from Brine Using a Desal Nanofiltration Membrane," *Journal of Water Process Engineering* 7 (2015): 210–217, https://doi.org/10.1016/j.jwpe.2015.06.012.

96. Y. Li, Y. J. Zhao, H. Wang, and M. Wang, "The Application of Nanofiltration Membrane for Recovering Lithium from Salt Lake Brine," *Desalination* 468 (2019): 114081, https://doi.org/10.1016/j.desal.2019.114081.

97. H. Li, Y. Wang, T. Li, et al., "Nanofiltration Membrane with Crown Ether as Exclusive Li+ Transport Channels Achieving Efficient Extraction of Lithium from Salt Lake Brine," *Chemical Engineering Journal* 438 (2022): 135658, https://doi.org/10.1016/j.cej.2022.135658.

98. A. Aghaei, A. Rahimpour, and M. Sadrzadeh, "Tailored L-Arginine Modified Poly(Piperazine-Amide) Nanofiltration Membrane with Enhanced Water Permeability for Efficient Li+/Mg2+ Separation," *Journal of Membrane Science* 728 (2025): 124140, https://doi.org/10.1016/j.memsci.2025.124140.

99. F. Yuan, Q. Wang, P. Yang, and W. Cong, "Transport Properties of Amino Acid Ions at Isoelectric Point in Electrodialysis," *Separation and Purification Technology* 168 (2016): 257–264, https://doi.org/10.1016/j.seppur.2016.05.058.

100. C. A. Fitch, G. Platzer, M. Okon, B. E. Garcia-Moreno, and L. P. McIntosh, "Arginine: Its p Ka Value Revisited," *Protein Science* 24 (2015): 752–761, https://doi.org/10.1002/pro.2647.

101. C. Y. Tang, Y. Zhao, R. Wang, C. Hélix-Nielsen, and A. G. Fane, "Desalination by Biomimetic Aquaporin Membranes: Review of Status and Prospects," *Desalination* 308 (2013): 34–40, https://doi.org/10.1016/j.desal.2012.07.007.

102. S. Tomita, H. Yoshikawa, and K. Shiraki, "Arginine Controls Heat-Induced Cluster–Cluster Aggregation of Lysozyme at around the Isoelectric Point," *Biopolymers* 95 (2011): 695–701, https://doi.org/10.1002/bip.21637.

103. Y. I. Sal'Nikov, G. A. Boos, V. V. Neklyudov, S. G. Fattakhov, and M. M. Shulaeva, "2, 4, 6-triaminopyrimidine and Its Associates with Bis (hydroxymethyl) Phosphinic Acid. State in Solution, Protolytic, and Complexing Properties," *Russian Journal of General Chemistry* 82 (2012): 1999–2004.

104. J. Kamcev, D. R. Paul, and B. D. Freeman, "Equilibrium Ion Partitioning between Aqueous Salt Solutions and Inhomogeneous Ion Exchange Membranes," *Desalination* 446 (2018): 31–41, https://doi.org/10.1016/j.desal.2018.08.018.

105. J. Kamcev, M. Galizia, F. M. Benedetti, et al., "Partitioning of Mobile Ions between Ion Exchange Polymers and Aqueous Salt Solutions: Importance of Counter-Ion Condensation," *Physical Chemistry Chemical Physics* 18 (2016): 6021–6031.

106. R. Lunkad, P. Biehl, A. Murmiliuk, et al., "Simulations and Potentiometric Titrations Enable Reliable Determination of Effective p Ka Values of Various Polyzwitterions," *Macromolecules* 55 (2022): 7775–7784, https://doi.org/10.1021/acs.macromol.2c01121.

107. D. Garrett, *Handbook of Lithium and Natural Calcium Chloride*, (Elsevier, 2004).

108. V.-D. Dang and M. Steinberg, "Preliminary Design and Analysis of Recovery of Lithium from Brine with the Use of a Selective Extractant," *Lithium Needs and Resources* 1978 (1977): 325–336.

109. L. Zhao, Y. Cheng, J. Hu, Q. Wu, and T. Xu, "Host–Guest Chemistry of Dendrimer–Drug Complexes. 3. Competitive Binding of Multiple Drugs by a Single Dendrimer for Combination Therapy," *The Journal of Physical Chemistry B* 113 (2009): 14172–14179, https://doi.org/10.1021/jp907437e.

110. M. Santo and M. A. Fox, "Hydrogen Bonding Interactions between Starburst Dendrimers and Several Molecules of Biological Interest," *Journal of Physical Organic Chemistry* 12 (1998): 293–307, https://doi.org/10.1002/(SICI)1099-1395(199904)12:4%3c293::AID-POC88%3e3.0.CO;2-Q.

111. S. Y. Zheng, J. Zhou, M. Si, et al., "A Molecularly Engineered Zwitterionic Hydrogel with Strengthened Anti-Polyelectrolyte Effect: from High-Rate Solar Desalination to Efficient Electricity Generation," *Advanced Functional Materials* 33 (2023): 2303272, https://doi.org/10.1002/adfm.202303272.

112. B. Yuan, Y. Zhang, P. Qi, et al., "Self-Assembled Dendrimer Polyamide Nanofilms with Enhanced Effective Pore Area for Ion Separation," *Nature Communications* 15 (2024): 471, https://doi.org/10.1038/s41467-023-44530-2.

113. S. A. M. Abou-alfitooh, A. S. Mohamed, F. M. Abdelhafiz, A. Zahran, and R. Hosny, "Enhanced Oil Recovery from Sandstone Reservoir Using Cationic Hyperbranched Polyamidoamine Dendrimer Surfactant

Flooding under Real Reservoir Conditions," *Scientific Reports* 15 (2025): 32509, https://doi.org/10.1038/s41598-025-17757-w.

114. M. Zhang, H. Yang, J. Wu, et al., "Dual-Responsive Nanotubes Assembled by Amphiphilic Dendrimers: Controlled Release and Crosslinking," *Materials* 13 (2020): 3479, https://doi.org/10.3390/ma13163479.

115. K. Borse and P. Shende, "Dendrimer-Mediated Proton Sponge Effect in the Treatment of Pulmonary Acidosis," *Drug Delivery and Translational Research* 15 (2024): 2547–2564, https://doi.org/10.1007/s13346-024-01752-1.

116. J. Wang, B. Li, L. Qiu, X. Qiao, and H. Yang, "Dendrimer-Based Drug Delivery Systems: History, Challenges, and Latest Developments," *Journal of Biological Engineering* 16 (2022): 18, https://doi.org/10.1186/s13036-022-00298-5.

117. L. Zhu, H. Yang, T. Xu, L. Wang, J. Lei, and C. Si, "Engineered Nanochannels in MXene Heterogeneous Proton Exchange Membranes Mediated by Cellulose Nanofiber/Sodium Alginate Dual Crosslinked Networks," *Advanced Functional Materials* 35 (2025): 2419334, https://doi.org/10.1002/adfm.202419334.

118. Z. Yu, X. Li, X. Li, et al., "Nacre-Inspired Metal-Organic Framework Coatings Reinforced by Multiscale Hierarchical Cross-Linking for Integrated Antifouling and Anti-Microbial Corrosion," *Advanced Functional Materials* 33 (2023): 2305995, https://doi.org/10.1002/adfm.202305995.

119. S. Gao, Y. Zhu, J. Wang, F. Zhang, J. Li, and J. Jin, "Layer-by-Layer Construction of Cu 2+ /Alginate Multilayer Modified Ultrafiltration Membrane with Bioinspired Superwetting Property for High-Efficient Crude-Oil-in-Water Emulsion Separation," *Advanced Functional Materials* 28 (2018): 1801944, https://doi.org/10.1002/adfm.201801944.

120. X. Li, C. Zhang, S. Zhang, J. Li, B. He, and Z. Cui, "Preparation and Characterization of Positively Charged Polyamide Composite Nanofiltration Hollow fiber Membrane for Lithium and Magnesium Separation," *Desalination* 369 (2015): 26–36, https://doi.org/10.1016/j.desal.2015.04.027.

121. M. Awais Ashraf, X. Li, J. Wang, S. Guo, and B. H. Xu, "DiaNanofiltration-Based Process for Effective Separation of Li+ from the High Mg2+/Li+ Ratio Aqueous Solution," *Separation and Purification Technology* 247 (2020): 116965, https://doi.org/10.1016/j.seppur.2020.116965.

122. W. Li, C. Shi, A. Zhou, X. He, Y. Sun, and J. Zhang, "A Positively Charged Composite Nanofiltration Membrane Modified by EDTA for LiCl/MgCl2 Separation," *Separation and Purification Technology* 186 (2017): 233–242, https://doi.org/10.1016/j.seppur.2017.05.044.

123. S. Jia, J. Wei, X. Ma, and Z. Wang, "Fabrication of Enhanced Mg2+/Li+-Selective Membranes via Aminoacetonitrile-Modulated PEI/TMC Interfacial Polymerization," *Desalination* 617 (2026): 119439, https://doi.org/10.1016/j.desal.2025.119439.

124. H. Wu, H. Zhao, Y. Lin, et al., "Positively-Charged PEI/TMC Nanofiltration Membrane Prepared by Adding a Diamino-Silane Coupling Agent for Li+/Mg2+ Separation," *Journal of Membrane Science* 672 (2023): 121468, https://doi.org/10.1016/j.memsci.2023.121468.

125. S. Zhang, T. Gu, Z. Li, et al., "Guanidinium Covalent Organic Framework Modulated Positively Charged Polyamide Membranes toward Superior Li+/Mg2+ Selectivity," *Journal of Membrane Science* 725 (2025): 124046, https://doi.org/10.1016/j.memsci.2025.124046.

Supporting Information

Additional supporting information can be found online in the Supporting Information section.

Supporting file: adfm73708-sup-0001-SuppMat.docx.